Light Collection Efficiency Simulations inside the Xenoscope Time Projection Chamber

Bachelor Thesis in Physics

Author
Hakan Ekinci

Supervised by
Prof. Dr. Laura Baudis
Dr. Jose Javier Cuenca García
Ph.D. Andrea Paloma Cimental Chávez

April 2026

Acknowledgments

I express my deepest gratitude to Prof. Dr. Laura Baudis for welcoming me into her research group to complete my Bachelor thesis. I am very thankful that she allowed me to work on this interesting project and that I was given such a unique opportunity to contribute to this field of research.

I am extremely grateful to my supervisor, Dr. Jose Javier Cuenca García for his continuous guidance, constructive feedback, and encouragement during the course of this project. His patience, commitment, and expertise were crucial for the completion of my thesis.

I also would like to thank my other supervisor Andrea Paloma Cimental Chávez for introducing me to this topic and for providing necessary help in the beginning of my thesis. The knowledge I have gained thanks to both of my supervisors is incredibly valuable to me.

Furthermore, I wish to thank my friends for their support in creating productive discussions which were very essential for the completion of this thesis.

Lastly, I would like to thank the reader of my Bachelor thesis for taking the time to read this work and I hope it will provide an interesting and insightful read.

Abstract

Observational evidence confirms the existence of dark matter, a type of matter that interacts mainly through gravity but could still interact with regular matter very weakly. Understanding the nature of dark matter remains a central objective in modern physics. While past and ongoing experiments have placed constraints on the mass and interaction cross-sections of various candidates, a direct detection of dark matter particles has yet to be made. A leading technology in the detection of Weakly Interacting Massive Particles (WIMPs), one of the most promising dark matter candidates, is the dual-phase time projection chamber (TPC) that employs liquid and gaseous noble elements as target medium.

This work focusses on the Xenoscope TPC, a dedicated test facility for the future large scale dark matter observatory of the XENON-LUX-ZEPLIN-DARWIN (XLZD) collaboration. Xenoscope is designed to investigate electron drift over the entire TPC length of 2.6 m, along with other key studies, such as the analysis of electron cloud diffusion. This thesis evaluates and characterises the photon detection efficiency of the Xenoscope TPC to determine its overall optical performance. To this end, a detailed Geant4-based Monte Carlo simulation of the TPC including all components was developed to model scintillation photon transport. Using the Geant4 framework, the Light Collection Efficiency (LCE) of the TPC was evaluated as a function of the initial vertical emission position. To achieve this, multiple photon simulations at different depths were performed, and resulting photon hits on the SiPM array were analysed. Additionally, the study evaluated whether the photons travelling through the liquid xenon are significantly deflected from their initial emission direction, focussing on the subset that successfully reached a detector element.

The data obtained from the simulations were parameterised using a fit consisting of a sum of two exponential functions that could follow the data points with high precision. The LCE as a continuous function of the vertical emission height was extracted from the fit parameters, providing a detailed characterisation of the optical performance of the TPC. A maximum LCE value of $\approx 0.7\%$ was achieved when photons were emitted directly below the interface between liquid and gaseous xenon. Furthermore, it was observed that photons which would reach the detectors were not significantly scattered and propagated upon emission almost directly towards the detectors. From this observation one concludes that strongly scattered photons cannot reach the detectors. Based on this result, incorporating reflector elements on high absorbing elements inside the TPC may enable the detection of photons that deviate significantly from their initial emission trajectory.

Contents

List of Figures

List of Tables

Overview

While the Standard Model of particle physics successfully describes the fundamental constituents of ordinary, so called baryonic matter, and their interactions, astrophysical evidence indicates that baryonic matter makes up only a small fraction of the energy budget of the universe. To resolve discrepancies in gravitational observations, the existence of an additional component, known as dark matter, is postulated. Dark matter is characterised by its significant gravitational influence and its lack of electromagnetic interaction, meaning it does not absorb, reflect, or emit light. However, current theories suggest it may still interact very weakly with baryonic matter through an unknown interaction type. One of the greatest scientific goals of our time is to detect dark matter and understand how it interacts. Many candidates for the constituents of dark matter have risen, but none of them have been detected so far. Some experiments searching for dark matter have already been conducted. The direct detection of dark matter interactions requires detectors sensitive to interactions with cross-section in the order of at least $10^{-48}\,\mathrm{cm}^2$ while being resilient to background. The dual-phase time projection chambers have emerged as one of the leading technologies in astroparticle physics, enabling three dimensional particle tracking within large target volumes. Past direct detection experiments could create a boundary on the interaction cross-section of dark matter particles with baryonic matter, raising the need for larger and more sensitive setups. To build the next generation dual-phase TPCs, extensive research and development (R&D) has to be carried out.

The Xenoscope facility at the University of Zurich serves as a dedicated R&D platform. It houses a demonstrator TPC designed to study optical and charge signal behaviour. Although smaller in overall volume, it is constructed to the full 2.6 m z-scale of the planned next-generation detectors, allowing this knowledge to be directly applied to their development. This Bachelor thesis focusses on the characterisation of the Light Collection Efficiency (LCE) of the Xenoscope TPC. The LCE defines the fraction of total scintillation photons produced by an event within the TPC volume that successfully reach and are recorded by the optical sensors. Specifically, a Geant4-based Monte Carlo simulation was developed to study the LCE.

The thesis is structured as follows: Chapter 1 provides the theoretical background on dark matter. Chapter 2 describes the working principles of a dual-phase TPC. Chapter 3 introduces the Xenoscope facility. Chapter 4 explains the Geant4 simulation framework. Chapter 5 presents the results of the optical photon simulations, focussing on the LCE and scattering effects. Chapter 6 discusses the conclusions obtained from the results and provides a future outlook.

1 Introduction

Dark matter remains one of the most profound mysteries of modern physics. To provide context for the work of this thesis, this Chapter gives a brief introduction to dark matter. It reviews a collection of historical and modern observational evidence, explores viable candidates, and mentions detection methods designed to measure its interactions with baryonic matter.

1.1 Observational Evidences of the Existence of Dark Matter

The hypothesis of dark matter does not stem from a single anomalous result, but rather from diverse astrophysical and cosmological observations. Because dark matter does not interact electromagnetically, its presence has been inferred through its gravitational effects on visible matter, light, and large-scale structures of the universe, as well as its imprints on the cosmic microwave background and from the Big Bang nucleosynthesis.

1.1.1 Application of the Virial Theorem to the Coma Cluster

In 1933, the Swiss astronomer Fritz Zwicky applied the virial theorem to observations of the Coma Galaxy Cluster. From observing the motion of individual galaxies inside the cluster he obtained their velocities. He then used these velocities of the galaxies to compute the total mass content of the cluster by applying the virial theorem. Further on, he estimated the total mass of the cluster by counting the luminous matter inside the cluster and calculating the masses. He found that the mass derived from the velocities of the galaxy was roughly 400 times greater than the luminous mass. The total mass obtained from counting luminous matter could not explain the measured velocities and was much lower than expected. In fact, the galaxies were moving far too fast to be held together by the luminous mass alone. The solution he introduced was that there must be additional non-luminous matter contained within this cluster gravitationally bound with the visible matter that makes up the discrepancy. He introduced the term dark matter to describe the non-visible matter contribution. Later observations of different galaxies came to the same results [68].

1.1.2 Rotational Velocities of the Galaxies

Further evidence was provided by Vera Rubin in 1970. She studied the rotation of spiral galaxies by measuring the velocities of stars and gas clouds at varying distances from the galactic centre. Classical physics predicts that objects would move slower the farther they are from the galactic centre. In contrast, the data showed that velocities did not drop off as expected, they plateaued and remained high even at the edge of the galaxy as seen in Figure 1. This big discrepancy did pose a problem. The galaxy should, in theory not be able to hold together maintaining such a high rotational velocity by its own gravitational pull. It became evident that a standard distribution of luminous matter could not sustain the observed velocities. The solution was that there must exist unseen matter in the galaxy distributed in such a way that it accounts for the discrepancy of the velocity curve. Decades after Zwickys discovery, a different observation came to the same conclusion. By introducing additional non-luminous dark matter distributed in the shape of a halo it was possible to explain why the velocities in the outer regions do not drop and why the galaxies were able to hold together [54].

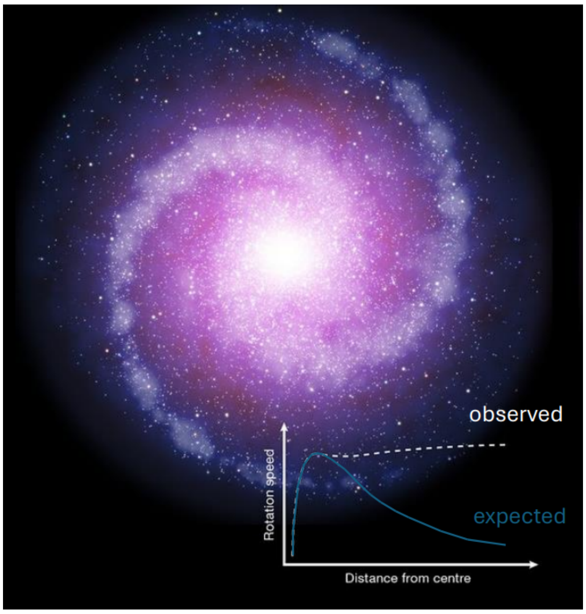

Figure 1: *Rotational velocities inside a galaxy as a function of distance from the galactic center. Note the discrepancy between the observed velocity curve from the visible disk (white) compared to the expected velocity curve computed from Keplerian orbits (blue). Modified from [32].*

1.1.3 Gravitational Lensing

According to general relativity, massive objects warp the spacetime around them. Unlike in Euclidean space, the shortest path between two points in this curved geometry is a curve rather than a straight line. Gravitational lensing occurs when light from a distant source bends around a massive object such as a star, galaxy, or galaxy cluster, following the curvature of spacetime generated by that mass. This effect allows light from objects hidden behind massive bodies to be bent in such a way that they become visible to an observer, as illustrated in Figure 2a. However, the apparent position on the sky of the lensed object is displaced from its true position. It is also possible that the object appears several times at different positions in the sky and that the shape of the object is distorted. The total mass of the body creating this lensing effect can be computed by analysing the distorted image of the background object. If one compares the total mass computed from gravitational lensing measurements to the visible collection of matter in the same region, a significant discrepancy occurs, meaning the total visible mass should not be able to bend the light from the object in the background as it is observed. From such an observation, the conclusion arises that the entire mass content of the lensing body is not visible. Gravitational lensing measurements of galaxies and galaxy clusters consistently show that the total mass inferred from the lensing signal exceeds the mass of luminous baryonic matter, meaning a significant amount of mass must stem from dark matter [43].

1.1.4 Anisotropies of the Cosmic Microwave Background

The possibly strongest indication of the existence of dark matter is given through the measurement of the cosmic microwave background (CMB), which was first discovered in 1964 by Arno Penzias and Robert Wilson [50]. The early universe after the Big Bang was a very opaque, dense and hot place. Photons created in the Big Bang could not travel through hot baryonic plasma and were experiencing a lot of scattering events. At around 380'000 years after the Big Bang the universe cooled down sufficiently that atoms could form and the universe became

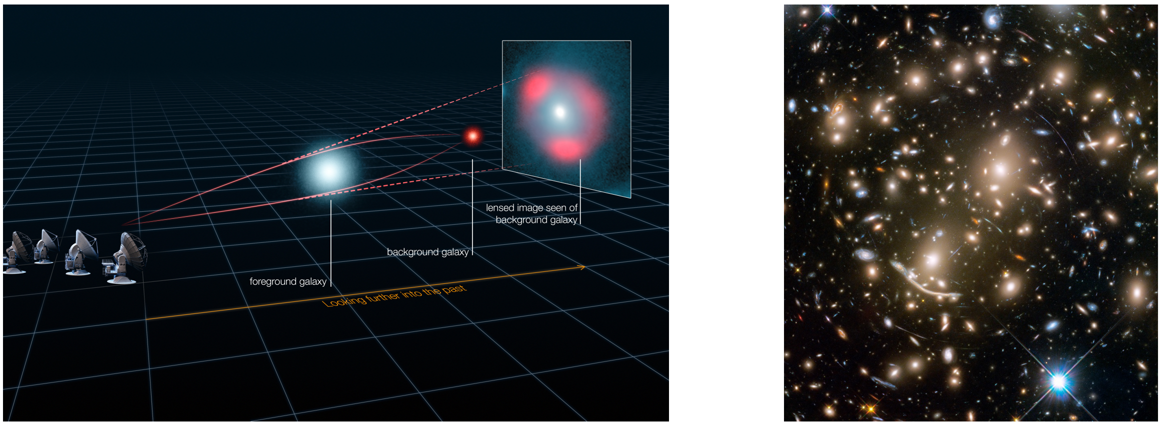

Figure 2: *a) Conceptual representation of gravitational lensing. The light of a background galaxy bends around a foreground massive galaxy and is reaching the observer leading to a distorted and displaced image of the real object. Figure taken from [33]. b) The galaxy cluster Abel 370 is acting as a gravitational lens for galaxies located behind the cluster. Distorted and discplaced images of the galaxies appear around the cluster. Figure taken from [46].*

transparent to these photons. In our time it is possible to measure these photons and, if measured, they will have a spectrum of wavelengths with a peak in the microwave range. The initial wavelengths of the photons released directly after the recombination phase was much shorter than measured today, but due to the expansion of the universe the wavelengths were shifted towards the microwave range. The observed wavelengths of the CMB are often translated into temperatures using the Wien displacement law, which leads to an average temperature of around 2.7 K nowadays. The temperature of the CMB is not perfectly uniform, it has small anisotropies which are temperature fluctuations in the order of 10^{-5} K. Satellites such as COBE 1992 [59], WMAP 2003 [11] and Planck 2013 [27] have measured the CMB in all directions and created a skymap of the CMB anisotropies. An example from Planck data can be seen in Figure 3. Those anisotropies encode information about the density fluctuations of baryons, dark matter, and the geometry of the universe at the time of the last scatter. By analysing these anisotropies, one obtains that baryonic matter contributes to around 5%, dark matter to around 25% and dark energy to around 70% of the total energy budget of the universe [57].

1.2 Dark Matter Classification

Traditionally, dark matter candidates have been categorised into three distinct regimes: cold [13], warm [42], and hot [52]. These classifications are determined by the velocity of the constituent particles relative to the speed of light during the era of structure formation. Cold indicates slower and hot being faster objects, whereas warm dark matter consists of elements in between.

Nowadays, hot and warm dark matter are excluded from the main constituent of dark matter because for the formation of the observed large scale structures a slower component for dark matter is required. Cold dark matter is therefore the leading candidate because its low primordial velocities naturally reproduce the observed large-scale structure of the Universe, matching CMB data and galaxy formation patterns with high precision. Combined with the concept of dark energy, the standard model for cosmology, the ΛCDM model arises, which is the modern theory of the universe. It explains the accelerating expansion of the universe, its large scale structure,

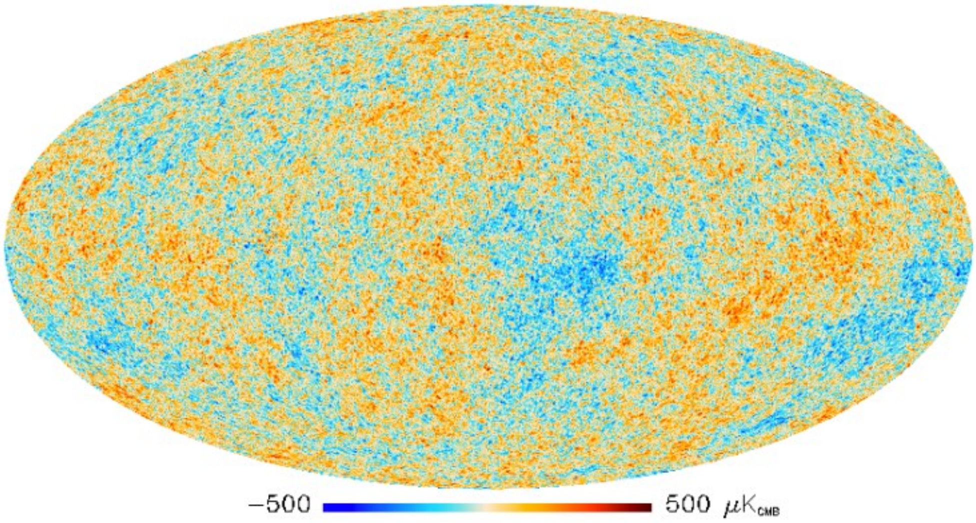

Figure 3: *A temperature map of the cosmic microwave background observed from Planck satellite. The temperature fluctuations of the CMB are in order of* 10^{-5} *K and Figure taken from [26].*

and the cosmic microwave background by attributing most of its energy content to dark energy Λ and cold dark matter (CDM) [13].

1.3 Dark Matter Candidates

There are several proposed candidates, which could be the constituent of dark matter. Most of them consist of a new type of particle beyond the Standard Model, unlike the first candidate, namely Massive Astrophysical Compact Halo Objects (MACHOs) that are compositions of baryonic particles. A selection of the most common candidates are listed here, note there are many more candidates. A brief overview of different candidates and their mass range can be found in Figure 4.

1.3.1 MACHOs

MACHOs consist of faint objects composed of baryonic matter that are not directly observable with optical telescopes, namely white and brown dwarfs, stellar black holes, and others. However, microlensing observations [4] and [5] showed that MACHOs cannot explain all phenomena from the section above on their own and would need more mechanisms to create a complete explanation. This leads to the conclusion that the constituent of dark matter must be of different type. Since baryonic matter is not able to explain all the phenomenons the true nature of dark matter must lie beyond the Standard Model of particle physics.

1.3.2 Axions

The axion [65] is a proposed bosonic candidate which solves the charge-parity (CP) problem of the strong force. It has been thought that the strong interaction conserves CP, however, there is no reason why this symmetry cannot be violated, as in the case of the Standard Model weak interaction where it is known that the CP operator is not conserved [61]. Although postulated to fix a Quantum Chromodynamics issue, axions turned out to have properties that make them suitable dark matter candidates. They are theorised to have masses in the µeV range and despite these stable, weakly interacting particles have such a low mass, they are expected to be nonrelativistic particles because their creation mechanism is non-thermal. Due to these properties, the axion matches the established profile of cold dark matter perfectly [40].

Up until today, no such particle has been detected. Microwave cavity experiments [58] are trying to directly detect axions.

1.3.3 Sterile Neutrinos

The sterile neutrino is the extension to the Standard Model neutrino which only appears with left-handed chirality. In contrast, the sterile neutrino is characterised to appear with the right-handed chirality [41]. Although their precise mass is unknown, sterile neutrinos are considered a prime candidate for dark matter. Observational bounds place their likely mass in the keV range [44]. This makes them significantly heavier than ordinary neutrinos but lighter than traditional cold dark matter candidates.

However, recent observations could not find any signature for sterile neutrinos in the mass range where they would make up all of dark matter [1].

1.3.4 WIMPs

The maybe most popular candidate for dark matter is the Weakly Interacting Massive Particle (WIMP). Based on the theory of Supersymmetry [56], the WIMP is thought to be a stable, new type of particle beyond the Standard Model that is created in the same way as baryonic particles through the Big Bang. In the early universe, WIMPs would have been in thermal equilibrium with ordinary matter. In this equilibrium state, a balance exists between WIMP annihilation and production. WIMPs annihilate to form Standard Model particles, and conversely, Standard Model particles interact to produce WIMPs. These annihilation and creation processes require that the WIMP must have a non-vanishing weak interaction cross-section to be able to exchange heavy gauge bosons with Standard Model particles. As the universe expanded and cooled, the annihilation rate of WIMPs fell, "freezing out" a relic abundance. This relic abundance naturally matches the correct amount of expected dark matter in the universe [22, 53]. The mass of a WIMP particle is estimated in the GeV and TeV range [38]. Since it is a massive particle it also interacts with baryonic matter particles via the gravitational force. These properties make the WIMP an excellent candidate for CDM.

The WIMP is a very promising candidate, which is why this work will focus on the WIMP model.

1.4 Distribution of Dark Matter in the Universe

Dark matter is thought to make up around 25% of the entire energy content of the universe [27]. In the early phase of the universe the baryonic and dark matter particles were distributed almost evenly in space with the exception of microscopic density fluctuations according to the CMB. Cosmological simulations such as the Millennium Run [60], MillenniumTNG [49], and IllustrisTNG [45] were conducted to analyse, among other phenomena, the evolution of matter and the emergence of large-scale structures in the universe. The results were that dark matter accumulates in a gigantic web like structure creating filaments, nodes and empty space. Baryonic matter is mainly accumulated inside this cosmic web, creating large scale structures that match with current observations. A visualisation can be found in Figure 5.

Overdense regions of dark matter inside filaments can collapse locally due to gravity into spherically shaped regions of higher dark matter density, these regions are called halos. Once

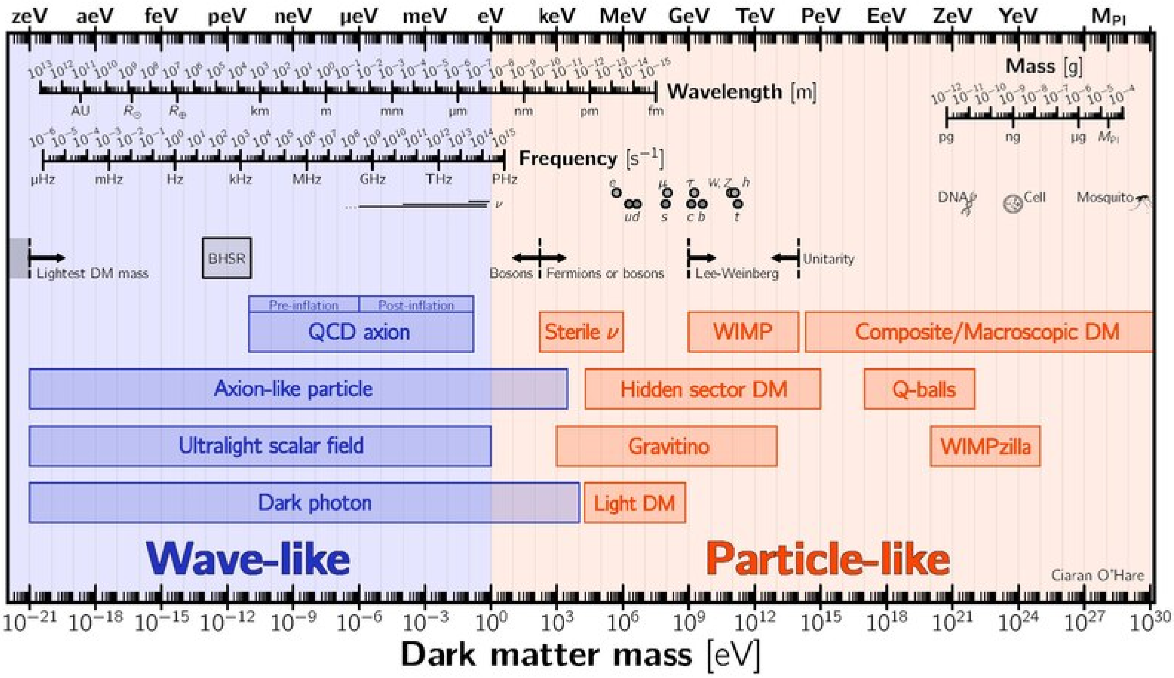

Figure 4: *An overview of different dark matter candidates postulated from various theories and their respective mass range in eV. The masses are ranging from ultralight wave-like particles to macroscopic candidates which behave more particle-like. The chart indicates the transition from particles behaving more wave-like to particle-like, from knowledge taken by Standard Model particles. Figure taken from [47].*

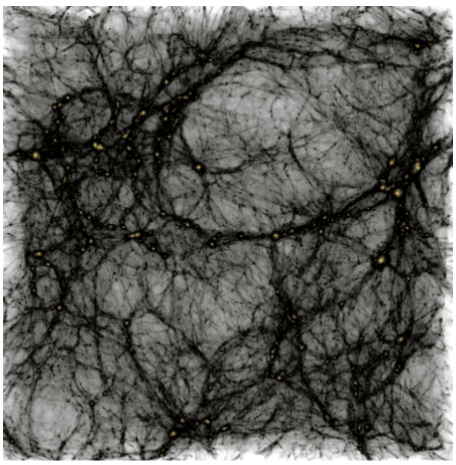

Figure 5: *Visualisation of the cosmic dark matter web structure. Dark matter is located inside filaments. The filaments cross at nodes which are regions of higher matter density. The empty regions are also called voids. The colored dots inside nodes illustrate baryonic matter. Figure taken from [64].*

a dark matter halo has formed, baryonic matter, mainly gas composed of hydrogen and helium falls into its potential well. Inside the halo, the baryonic matter is drifted towards the centre, where if the halo is sufficiently massive, galaxies or galaxy clusters can form. A dark matter halo extends much further into space than the visible galaxy itself [64]. In the case of the Milky Way where the visible galaxy extends to around 15 kPC from the galactic centre the halo extends to around 200 kPc [63]. An artistic impression can be seen in Figure 6. In the centre of the image the Milky Way Galaxy is presented. The dark matter halo is indicated by a blue colour around the galaxy.

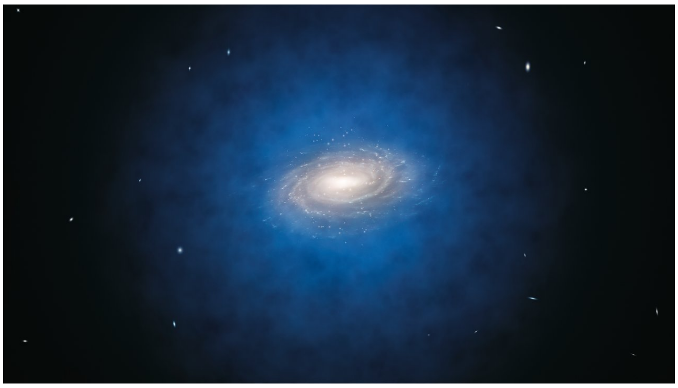

Figure 6: *An artistic impression of the Milky Way Galaxy with its dark matter halo visualised in blue colour. Figure taken from [34].*

Similarly, as discussed in Section 1.1.2 it is possible to measure the rotational curve of the Milky Way and compare the measurement with the expected matter mass inside the galaxy to gain an estimate on the dark matter content of the Milky Way [39]. In general, the local dark matter density is estimated to be around $\rho_0 = 0.3\,\mathrm{GeV\,cm^{-3}}$.

In summary, it is expected that dark matter is distributed in the entire universe. Recent theoretical studies suggest the existence of a local dark matter densities in the vicinity of the orbit of the earth [51]. It seems possible that detectors on earth could detect such a particle.

1.5 Dark Matter Direct Detection

Experimental searches for WIMPs rely on three strategies: indirect detection, collider production, and direct detection.

Indirect detection focusses on astrophysical environments with high dark matter densities, such as the galactic centre or the sun. In these regions, WIMPs may self-annihilate or decay, producing a flux of observable Standard Model particles. The aim is to observe peaks in the particle flux signal that deviate from the expected spectrum, which allows for the reconstruction of the WIMP mass and its annihilation cross-section.

Collider searches conducted at the Large Hadron Collider (LHC) [35] aim to produce dark matter particles in controlled high-energy proton-proton collisions. Since WIMPs are electrically neutral and weakly interacting, they would escape the detector without depositing energy. By summing the momentum vectors of all detected particles and comparing the result to the initial beam energy, one can calculate the missing energy carried away by the WIMP by applying the law of conservation of energy and momentum.

Lastly, direct detection, which is the primary focus of this work, aims to observe the scattering of WIMPs off a Standard Model atomic nuclei within detectors with a target material.

As discussed in previously the Milky Way is embedded in a dark matter halo. While the solar system orbits the galactic centre the earth traverses the halo effectively receiving a flux of WIMPs passing through the earth. The average velocity of these particles relative to earth is estimated to be around 220 km/h. As theories suggest there is an non-vanishing interaction cross-section mediated by an unknown mediator between Standard Model particles and WIMPs. The concept of direct detection is to measure the elastic scattering as seen in Figure 7 between a WIMP coming from this halo and a target material located inside a detector on earth. The energy can be transferred primarily to the atomic electrons or to the nucleus. The struck particle is set into motion, this process is called a recoil. Recoils are classified as either electronic recoils when the energy is imparted to electrons or nuclear recoils when the energy is transferred to the nucleus. A WIMP with mass m_χ is expected to interact with the nucleus with mass m_A. When it does so, it transfers a small amount of kinetic energy E_{NR} in the order of keV to the target nucleus. This energy deposition is further on released by the target through one or a combination of three excitation channels, namely heat, ionisation, or light which can be collected by detectors [12].

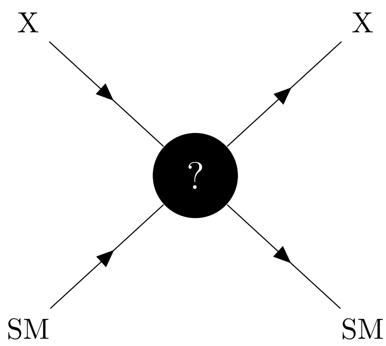

Figure 7: *Schematic overview of a scattering event between a Standard Model particle (SM) and a WIMP (χ).*

The differential rate of WIMPs from the dark matter halo scattering off a target nucleus can be estimated by the following equation:

$$\frac{dR}{dE_{NR}} = \frac{\rho_0 M}{m_A m_\chi} \int_{v_{min}}^{v_{esc}} v f(v) \frac{d\sigma}{dE_{NR}} dv \tag{1}$$

where ρ_0 denotes the local dark matter density, M is the total mass of the detector target medium, v_{min} is the minimum velocity of the WIMP particle to induce a nuclear recoil, v_{esc} is the escape velocity of the Milky Way, $f(v)$ is the normalised WIMP velocity distribution inside the halo defined by the Maxwell-Boltzmann distribution, σ is the interaction cross-section between WIMP and target [15, 56]. From Equation 1 it is visible that some contributions to the rate cannot be influenced such as the local density, WIMP mass, etc, which are given from the properties of the universe. Experimentally, the expected event rate can only be maximised by optimising the choice of target material and increasing the total mass of the detector. In Figure 8 the rate is plotted for different values of the recoil energy E_{NR} for different target materials. One can see that in the lower to moderate recoil energy regimes xenon is an excellent target material, expecting the most rate of interaction. In higher recoil energy regions, materials such as germanium are expected to have a higher rate. Additionally, the cross-section of a spin-independent interaction between a WIMP and target nuclei with atomic mass number A is related as $\sigma \propto A^2$. Spin-independent means that the interaction does not depend on the spin state of either of the participants. It is therefore useful to employ heavy targets with a high atomic mass number such as xenon in spin-independent direct detection experiments to maximise the cross-section.

Generally, there is also a spin-dependent contribution to the cross-section, but unlike the spin-independent part, it is mainly driven by the nuclear spin structure, coupling only to unpaired nuclear spins and does not scale with atomic mass [12, 15].

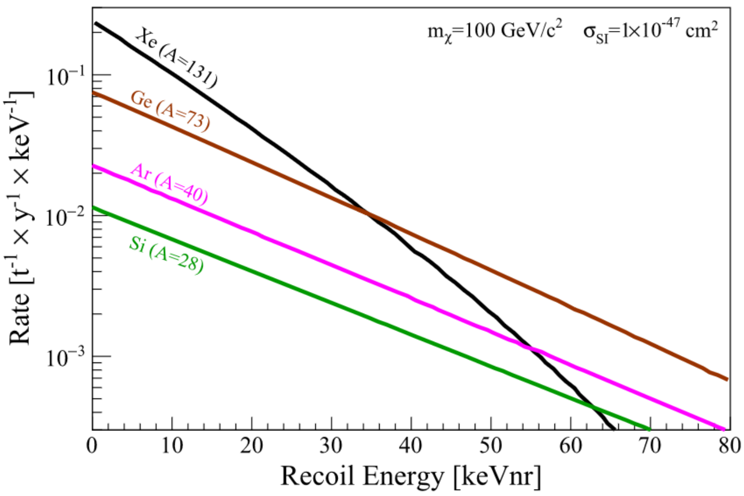

Figure 8: *Nuclear recoil spectra induced by a $m_\chi = 100$ GeV WIMP in various target materials with atomic mass numbers A. The assumed spin-independent interaction cross-section was $\sigma = 10^{-47} cm^2$. Figure taken from [56].*

In the next Chapter, the dual-phase time projection chamber is presented. This is a key tool for dark matter direct detection experiments and the main focus of this thesis.

2 Dual-Phase Time Projection Chamber

A dual-phase time projection chamber (TPC) is a highly sensitive particle detector widely used in experiments looking for various rare events, such as dark matter interactions or neutrino scattering. It operates with a noble element, typically xenon or argon. In this work, the focus will be on a TPC that contains liquid (LXe) and gaseous xenon (GXe).

2.1 Properties of Liquid Xenon

Some properties of xenon relevant for rare-event searches are listed in Table 1.

Property	**Value**
Atomic number Z	54
Mean atomic mass	$131.29\,\mathrm{g\,mol^{-1}}$
Liquid density	$2.94\,\mathrm{g\,cm^{-3}}$
Scintillation wavelength	175 nm
Scintillation light yield (at 122 keV)	63 Photons per keV
Boiling temperature	165.0 K
Melting temperature	161.4 K
Gas density at 1 atm and 298 K	$5.40\,\mathrm{g\,L^{-1}}$
Gas density at 1 atm and 165 K	$9.99\,\mathrm{g\,L^{-1}}$

a)

Isotope	**Abundance (%)**	**Half-life ($T_{1/2}$)**
^{124}Xe	0.095	$1.1 \cdot 10^{22}$ yr
^{126}Xe	0.089	$> 1.9 \cdot 10^{22}$ yr
^{128}Xe	1.91	Stable
^{129}Xe	26.4	Stable
^{130}Xe	4.07	Stable
^{131}Xe	21.18	Stable
^{132}Xe	26.9	Stable
^{134}Xe	10.4	$> 8.7 \cdot 10^{20}$ yr
^{136}Xe	8.86	2.16×10^{21} yr

b)

Table 1: Overview of xenon properties. (a) General physical properties of xenon. (b) Natural isotopic abundance and half-lives. Values taken from [6] and [9].

Some of the following properties make xenon an excellent target medium for particle interactions:

- **Atomic Number and Density:** Xenon is a heavy noble gas characterised by a high atomic number ($Z = 54$) and a high density in the liquid phase ($\approx 3\mathrm{g\,cm^{-3}}$). As previously discussed, its large mass number A is beneficial for direct detection because the interaction cross-section scales as $\sigma \propto A^2$. The high density (comparable to that of aluminium) creates a strong self-shielding against external radiation [6, 9].

- **Radioactive Isotopes:** The lifetimes of the xenon isotopes listed in Table 1b are so long that the overall background caused by these rare decays is very low, though specific processes like the double electron capture of ^{124}Xe do produce a distinct, low-energy background that needs to be accounted for [6, 9].

- **Scintillation Properties:** LXe is also an excellent scintillator. A scintillation photon can be created through excitation (Xe^*) or ionisation (Xe^+) of a xenon atom. These processes can occur through an interaction of a particle with the nucleus or an atomic electron of xenon. In addition, xenon is transparent to its own scintillation light, which means that these photons can pass traverse the medium without being absorbed.

In principle two different modes of scintillation processes can happen. The first mode is given as the following:

$$\begin{aligned} \mathrm{Xe}^* + \mathrm{Xe} + \mathrm{Xe} &\rightarrow \mathrm{Xe}_2^* + \mathrm{Xe} \\ \mathrm{Xe}_2^* &\rightarrow 2\mathrm{Xe} + h\nu \end{aligned} \tag{2}$$

In this mode a particle interaction leads to an excitation of a xenon atom. This excited xenon atom can bond with another xenon atom and form an excited xenon dimer Xe_2^*. Upon deexcitation of the dimer the xenon returns to the ground state, breaking the bond and releasing a photon with the scintillation wavelength of 175 nm [9].

The second mode is described by the following processes:

$$\begin{aligned} \mathrm{Xe}^+ + \mathrm{Xe} &\rightarrow \mathrm{Xe}_2^+ \\ \mathrm{Xe}_2^+ + \mathrm{e}^- &\rightarrow \mathrm{Xe}^{**} + \mathrm{Xe} \\ \mathrm{Xe}^{**} &\rightarrow \mathrm{Xe}^* + \mathrm{heat} \\ \mathrm{Xe}^* + \mathrm{Xe} + \mathrm{Xe} &\rightarrow \mathrm{Xe}_2^* + \mathrm{Xe} \\ \mathrm{Xe}_2^* &\rightarrow 2\mathrm{Xe} + h\nu \end{aligned} \tag{3}$$

In this mode, the interaction of a particle with xenon leads to the ionisation of a xenon atom. The ionised xenon can be captured and bonds with a different xenon in the ground state and produces an ionised xenon dimer Xe_2^+. The free electron that gets produced can either escape or be captured by an ionised xenon dimer leading to a second order excited xenon atom. Then, this state returns to the first excited level, releasing heat. From this point on, the process continues in the same way as in the process 2, which leads to the release of the scintillation photon with wavelength of 175 nm [9].

Most importantly, particle interactions in LXe transport energy through two primary channels. The first is the emission of scintillation photons, while the second consists of ionised electrons that escape recombination. In addition to these channels, it is also possible that a particle interaction can deposit thermal energy in the form of heat in the LXe. A visualisation of these processes is shown in Figure 9. Crucially, a property of xenon is that it is transparent to its own scintillation light, meaning that it does not absorb the emitted photon. This transparency arises because the scintillation photon originates from the decay of an excited xenon dimer. Since the individual unbound xenon atoms are all in the ground state, they cannot absorb this photon [9]. Furthermore, xenon is considered a fast scintillator medium. The time interval between an interaction in LXe and the emission of scintillation light is either 2 ns or 27 ns, corresponding to the decay of the excited xenon dimer Xe_2^* in the first or second mode, respectively [6, 9].

Although LXe is transparent to its own scintillation light, propagating photons can still undergo Rayleigh scattering. This process describes the mechanism in which a photon elastically scatters off a particle that is smaller than its wavelength without losing energy altering its initial trajectory. In the case of the scintillation light of xenon, Rayleigh scattering occurs when these photons interact with the electron cloud of a xenon atom. The cross-section for such an interaction depends strongly on the wavelength of the photon described as $\sigma \propto \lambda^{-4}$. Because of this relationship, the scintillation photons produced in LXe are highly susceptible to Rayleigh scattering, making it the dominant mechanism for photon trajectory changes.

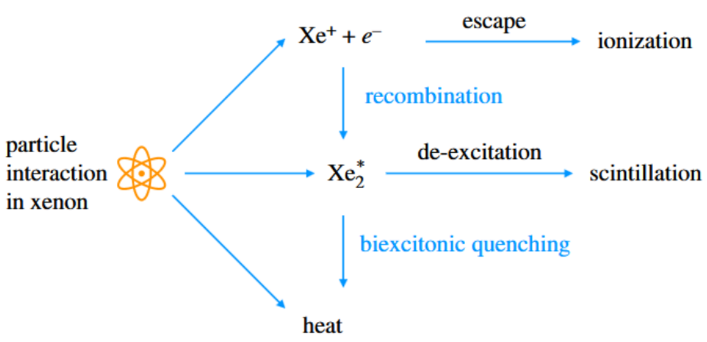

Figure 9: *Excitation and ionisation processes that occur after a particle interacts with LXe. Note that through a particle interaction with LXe the energy can be emitted through two main channels. The first one being a scintillation photon and the second one an ionised electron. Heat is also produced by the interaction, but cannot be detected in this setup. Figure taken from [9].*

2.2 The Working Principle of a Xenon Time Projection Chamber

A dual-phase xenon TPC is housed inside a cryostat and consists of a GXe layer located above a LXe target. The liquid volume is divided into an active region, which is instrumented with electric fields and photosensors to record particle interactions and a surrounding inactive region, which serves as a shield against external background radiation. A particle interaction with the active LXe leaves a trail of scintillation light and ionisation electrons as discussed in Subsection 2.1. The scintillation light traverses the medium and can be detected by the photosensors almost instantly after the interaction, creating the primary signal (S1). An applied homogeneous electric drift field controls the velocity of the ionisation electrons, drifting them upward through the active LXe until they reach the boundary between LXe and GXe. Upon reaching this interface, they are exposed to a different, much stronger electric field that accelerates the electrons and extracts them into the gas phase. In the GXe the accelerated electrons start to interact with the GXe where they create more scintillation photons in a cascade event via electroluminescence. These photons induce a secondary signal (S2) when they reach the detectors. The S2 signal strength is proportional to the number of ionisation electrons created by the initial particle interaction inside the LXe. A short time delay between the S1 and S2 signal gives rise to the amount of time that the electrons drifted upward. Knowing the drift velocity of the electrons and the drift time, it is possible to reconstruct the event position in the z-direction. The S2 signal is very localised on the x-y plane, which means that the position on which the secondary photons arrive to the detectors on the top indicates the initial position of the event on the x-y plane. Combining the information from the reconstructed x–y and z positions of the interaction allows the complete reconstruction of the location of the even in the three-dimensional space.

As motivated before, in liquid xenon detectors, incident particles deposit energy through collisions with the xenon atoms. The energy loss in LXe differs for different interaction types. A nuclear recoil gives a different amplitude of the S2 signal compared to an electronic recoil produced by background events. By analysing the ratio of amplitudes S2/S1 it is possible to distinguish between nuclear and electronic recoil signals [55]. For example, highly ionising electronic recoils from background radiation yield a significantly larger S2/S1 ratio than the nuclear recoils expected from dark matter interactions. The heat energy deposited by a particle

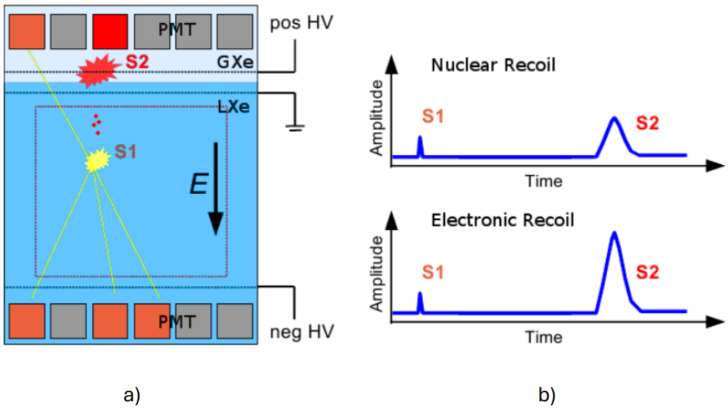

Figure 10: *A schematic overview of the working principle of a TPC. a) The setup of a TPC with photosensors on top and on the bottom. An interaction is visualised by the yellow dot and the straight lines indicate the path the scintillation photons take that create the S1 signal. The ionised electrons are drifted to the interface between LXe and GXe at which they are accelerated into the GXe creating more photons in the cascade interactions which generates the S2 signal. b) The amplitude difference between nuclear and electronic recoil signals is illustrated. A nuclear recoil results from a particle interacting with the xenon nucleus, whereas an electronic recoil arises from interactions with a bound electron. Figure taken from [55].*

interaction cannot be detected by this detector type and is therefore lost. A graphical overview of a dual phase xenon TPC can be seen in Figure 10.

2.3 Past, Present and Future Dark Matter Direct Detection Experiments

Experiments such as XENON100 [7], XENON1T [8], and LUX [36] have demonstrated the power of liquid xenon TPCs in achieving the low background levels and high-resolution event reconstruction required for rare event searches. These detectors rely, among other parameters, heavily on the efficient collection of scintillation and electroluminescence light, making the optical performance of the detector a critical design parameter. Current experiments such as LZ [23], XENONnT [28], and PandaX-4T [24], which contain 10, 8.6, and 5.6 tonnes of xenon respectively, have established new constraints on the WIMP mass and cross-section due to their high sensitivity. However, they did not manage to detect a signal from WIMP interactions. Consequently, future efforts in order to detect a dark matter recoil signal focusses on constructing even larger detectors to achieve sensitivities approaching closely the so-called neutrino fog. This term refers to an irreducible background of astrophysical neutrinos that induce nuclear recoils, indistinguishable from dark matter signals, which is why they represent a fundamental limit to direct detection sensitivity. The neutrino fog is not a hard limit on discoveries, but can be overcome with enough statistics [48]. The XLZD [66] collaboration proposed the next-generation multiton xenon detector, which requires extensive research and development to build. An overview of the exclusion areas created by various experiments can be found in Figure 11.

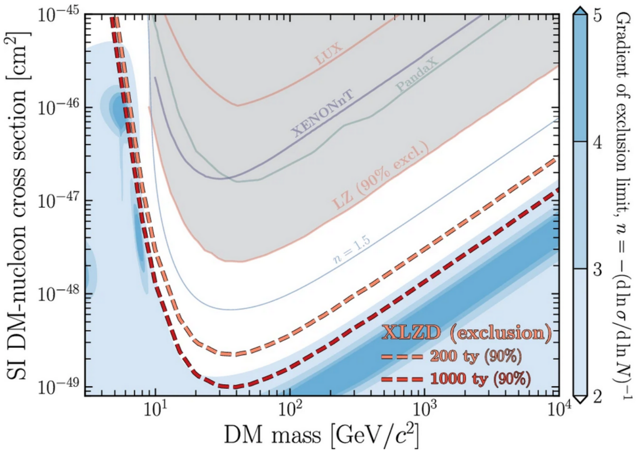

Figure 11: *Spin-independent WIMP-nucleon exclusion limits. The plot compares current exclusion limits from LUX, PandaX, XENONnT, and LZ with the projected sensitivity of XLZD. The colour gradient (from lighter to darker blue shades) shows the neutrino fog, a region where the discovery potential becomes systematically limited due to nuclear scattering of astrophysical neutrinos on xenon atoms. Figure taken from [66].*

3 The Xenoscope Time Projection Chamber

As briefly mentioned before, the next-generation WIMP detecting TPC, which will contain approximately 50 to 70 tons of liquid xenon is part of the XLZD collaboration [66]. It is still in its baseline design phase, but it is conceptualised as a vertical, cylindrical vessel with a diameter and height of 3 m.

Constructing such a large detector requires an extensive research and development programme. To this end, the Xenoscope facility was built that contains a 2.6 m tall dual-phase TPC, serving as a vertical demonstrator for future detectors. The main goals of Xenoscope are to demonstrate the drift of electrons in the liquid xenon over the distance of 2.6 m, to measure the diffusion of the electron cloud in longitudinal and transverse directions, as well as the optical properties of the medium [2]. In this Chapter, the construction of the Xenoscope TPC will be introduced.

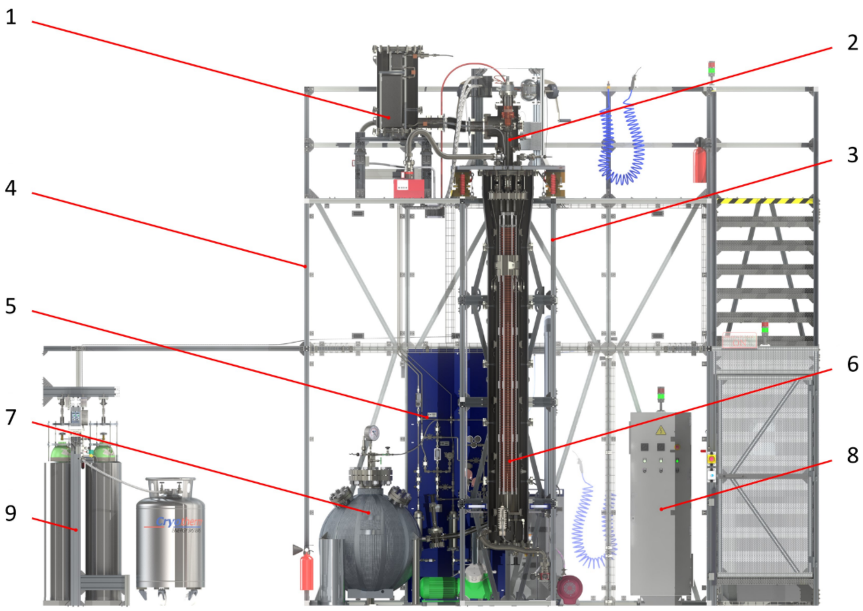

Figure 12: *Schematic view of the Xenoscope facility with the 2.6 m TPC installed in the double walled cryostat. Legend: (1) Heat exchanger, (2) Cooling tower, (3) Inner frame, (4) Outer frame, (5) Purification gas panel, (6) TPC in the 24.8 cm diameter and 312 cm height cryostat, (7) High-pressure storage vessel of liquid recovery system, (8) Power distribution cabinet, (9) The BoX, a gas recovery and storage system. Figure and legend taken from [10].*

3.1 Support Structure

The Xenoscope TPC as shown in Figure 12 is held by a support structure created by aluminium profiles. The support structure is divided into the inner and outer frames. The inner frame supports the entire weight of the cryostat and its content. The outer frame provides lateral support for the inner frame and for an upper level floor. A seperate third frame supports a stair access to the upper parts of the TPC for operation and assembly. The support frames fully enclose the cryostat assembly to minimise dust accumulation and can be accessed by two double doors [10].

3.2 Xenon Storage

The xenon gas handling system is connected to a dedicated recuperation system that allows recovery and storage of the xenon from the TPC during downtime. The xenon can be stored in 9 aluminium gas cylinders each storing 40 L up to a maximum of 418 kg of GXe. From these storage vessels, the GXe can be routed to the TPC and subsequently recovered for storage. A transfer to the storage and back can take a lot of time because the liquid xenon inside the TPC can only be evacuated by evaporating it into the gas phase, which makes it a long process if this has to be done often. In order to minimise the time to recover the xenon, a spherically shape storage vessel, called Ball of Xenon (BoX), exists that allows the direct recovery of liquid xenon. This special storage is kept cold and has enough capacity to contain 450 kg of liquid and gaseous xenon at a maximum pressure of 90 bar [10].

3.3 Cooling Tower and Heat Exchanger

The cooling tower, located on top of the cryostat, contains a PC-150 [62] pulse tube refrigerator from Iwatani. It ensures that the gaseous xenon coming from the storage moves through a getter to remove impurities and condenses into the liquid phase when entering the cryostat. It also regulates the overall temperature of the TPC to maintain LXe. The xenon is also purified during operation. To achieve this, liquid xenon is extracted from the top of the cryostat, evaporated into the gas phase, purified and re-condensed into the liquid phase and returned into the cryostat. The heat exchanger minimises the heat leak from the GXe during purification processes, reducing the overall heat increase in the TPC. It uses the heat from the warm, purified xenon gas returning to the main body to help evaporate the cold liquid xenon that is being extracted for purification. Similarly, it uses the cold outgoing LXe to cool down and liquify the warm incoming xenon gas before it re-enters the cryostat [10].

3.4 Cryostat

The cryostat houses the TPC and is made of a double walled stainless steel cylinder. The space between the inner and outer shell is under vacuum which eliminates heat transfer via conduction and convection from the room-temperature environment to the cold inner vessel. Moreover, it is designed to withstand the operating pressure of the system and to structurally support the TPC. The xenon target mass that can be contained within the cryostat is around 350 kg [10].

3.5 Field Cage

Inside of the inner cryostat shell is the TPC field cage, which consists of 173 oxygen-free, high thermally conductive copper rings as seen in Figure 13. The copper rings have an inner diameter of 16 cm and are held in place by six polyamide-imide pillars along the z-axis. The field cage establishes a uniform electric field, which directs the drift of electrons upwards towards the liquid and gas xenon interface. This uniformity is critical to ensure that ionisation electrons drift vertically from the liquid xenon volume up to the gas phase without their trajectories being distorted, which allows for accurate 3D position reconstruction of particle interactions. The field cage is not concentric to the inner vessel and is shifted off centre. A liquid-level monitoring and setting system is placed on the major clearance side. The xenon located inside the field cage is called the active volume. It is the main part of the xenon that acts as a target for interactions. The xenon lying outside of this field cage is defined as the inactive volume which can still act as a target, but signals created in that region would need to penetrate the field cage to reach the detectors [2, 10].

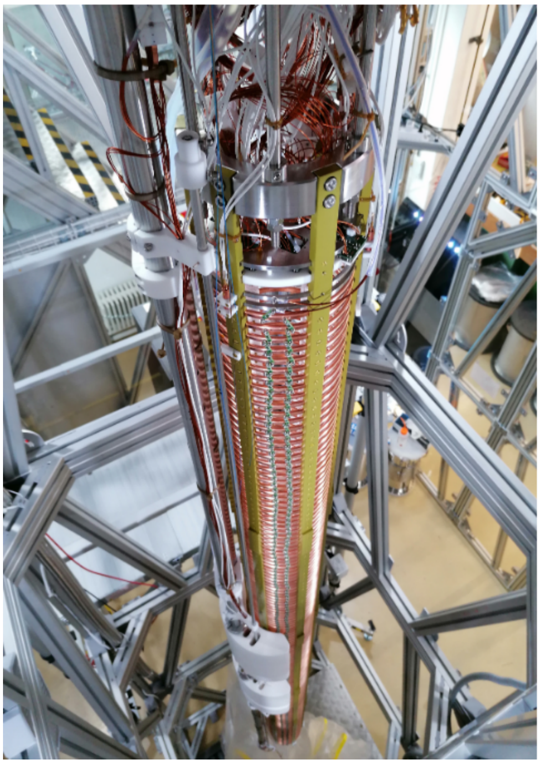

Figure 13: *The field cage of the Xenoscope TPC. The cage consists of 173 copper rings with an inner diameter of 16 cm mounted on polyamide-imide pillars along the vertical axis of the TPC. Figure taken from [2].*

3.6 Photosensors

The photosensors in the Xenoscope TPC serve as the optical readout system of the TPC, designed to convert the scintillation photons emitted by liquid xenon into measurable electrical signals. In this setup, the silicon photomultipliers S13371-6050CQ-02 [2] from Hamamatsu are used. The sensor array consists of a total of 192 multi-pixel photon counters, each 6×6 mm^2 in size. These sensors are bundled in groups of four into so called quad modules. In total 48 2x2 quad modules, as seen in Figure 14c are present. In turn, four of these quad modules are mounted onto a single readout PCB to create units known as tiles. A visualisation of cells, quads, and tiles can be found in Figure 14b. Each tile is labelled by a letter starting from A to M, excluding letter I as seen in Figure 14d. Since each of these tiles has its own readout channel, it is possible to distinguish exactly which tile received a photon hit. The tiles in addition serve as pre-amplifiers for the collected photon signals before further processing. In total, the area covered with active sensors is 36% [29] of the array surface. Furthermore, the photosensor array is mounted closely above the field cage inside the GXe to ensure the precise traceability of the S2 photons origins. SiPMs were selected for this configuration to ensure scalability for future upgrades if necessary. The current SiPM array allows for the distinction of 12 different regions. By increasing the number of readout channels in the backend, it is possible to refine the granularity. This allows for improved spatial resolution if future R&D phases demand it, without requiring mechanical modifications to the array surface.

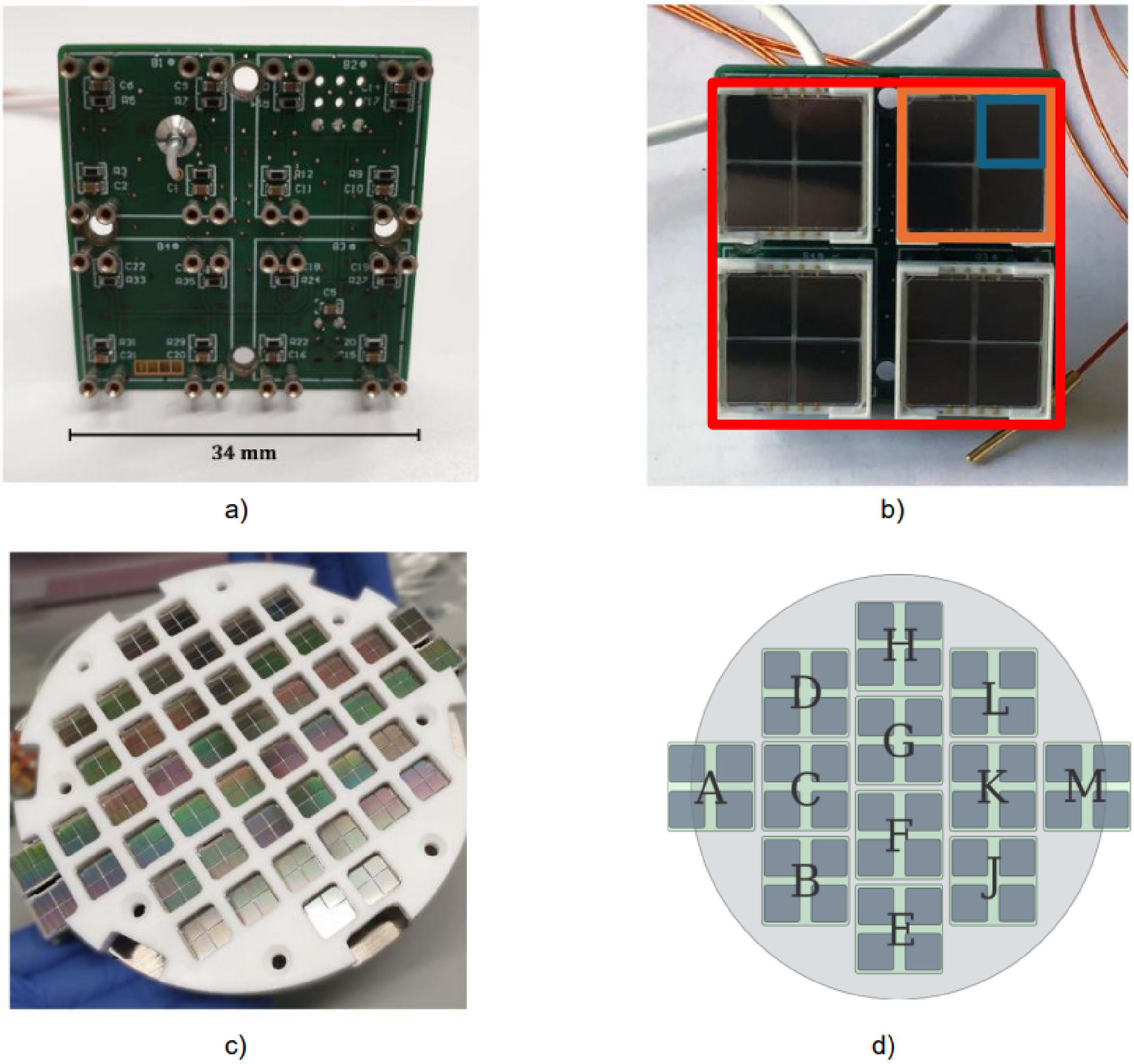

Figure 14: *a) Readout printed circuit board without mounted SiPMs. b) Picture of a single assembled SiPM readout channel. A cell (green) consists of a 6×6 mm^2 pixel counter. A quad (orange) is a collection of four cells. A tile (red) is a group of four quads mounted on the readout board. c) A picture of the fully assembled photosensor array with PTFE cover. Consists of 12 tiles. d) A graphical representation on how the quad modules are grouped for each read out channel with assigned letters starting from A to M, excluding the letter I. Figures taken and modified from [2] and [29].*

4 Geant4 Simulations of the Xenoscope Time Projection Chamber

Using the Geant4 toolkit, photon simulations inside the Xenoscope TPC were created. These simulations were critical for determining the Light Collection Efficiency of the TPC, providing the baseline needed to characterise the optical performance of the TPC. A detailed description of the applied methods and simulation framework used is provided in this Chapter.

4.1 Description of the Simulation Framework

The framework used in this thesis to create the simulations is called Geant4 [3]. This is a simulation tool developed by physicists and computer scientists at CERN to simulate the passage of particles through matter. Geant4 has established itself as the preeminent toolkit for particle physics, serving as the standard computational framework for major experiments such as those at the LHC. Beyond that, it is also applied in diverse fields, including medical physics for hadron therapy dosimetry or in aerospace engineering for optimising radiation shielding. Additionally, it is an excellent toolkit for creating simulations in rare event searches, such as dark matter interactions.

Geant4 is a toolkit that consists of a vast number of libraries which can be used to simulate physical interactions at microscopic levels. On top of the Geant4 libraries, a C++ code has to be created which defines the exact parameters of the experimental setup. Geant4 libraries include a wide variety of functionalities [20], such as the following:

- **Geometry Construction**: This consists of various shapes and physical volumes, including material properties of elements, isotopes, and complex compounds forming these volumes.
- **Particle Generator**: It is used to create specified particles inside a volume element. All properties of generated particles, such as energy, lifetime, location, or propagation directions, can be defined.
- **Detailed Physical Processes**: These include the simulation of particle interactions, such as electromagnetic or hadronic interactions and their cross-sections, Information on particle decay and the decay products, and particle transport in and between volumes.
- **Storage**: Enables the ability to store specified data such as interaction types, positions, momenta, energies, particle types, etc. which can then be used for further analysis.
- **Visualiser**: Creates the possibility to make graphical visualisations such as geometries, trajectories, etc.

The Geant4 toolkit organises the simulation of particle interactions into a strict hierarchical data structure. This hierarchy is designed to manage the stochastic nature of Monte Carlo methods efficiently. The Geant4 data structure is organised in four levels:

1. **The Run**: The highest level of the hierarchy is the Run. A Run includes the entire simulation for a specific configuration. At the initialisation of a `G4Run` class object, the detector geometry is constructed, the physics processes are defined, and the material properties are loaded into memory. The Run manages the global state of the simulation and consists of independent Events.

2. **The Event**: The fundamental unit of the simulation is the Event. A Run can be divided into several Events. The class object `G4Event` represents the full history of a particle interaction, from generation to termination, where the latter means that either particles are absorbed, decayed, or escape from the system.

3. **The Track**: Within an Event, each individual particle is represented by a Track. It is important to note that in Geant4, a `G4Track` does not represent the geometric path of the particle but, it is a class that contains the current physical state of the particle (energy, momentum, position, etc.). In addition to these properties, the Track contains information on the heritage (family tree analogy) of a particle through unique identifiers, namely the TrackID and ParentID. This data allows the simulation to distinguish between primary particles (generated at the source) and secondary particles (produced via interactions).

   - **The TrackID**: An integer number is assigned to each particle upon creation. This number is the so called TrackID. Primary particles (first generation of generated particles) are initialised with a TrackID of 1, while subsequent secondary particles are assigned sequential numbers (2, 3, etc.) as they are generated.

   - **The ParentID**: The TrackID of the specific particle that generated the current one via a physical interaction is recorded in the ParentID. Primary particles are assigned a ParentID of 0, while secondary particles inherit the TrackID of their creator.

4. **The Step**: The finest granularity of the simulation is the Step. A single Track contains all Steps a particle takes during its existence inside the system. The `G4Step` class defines the discrete information of the trajectory a particle takes between two key points:

   - **The PreStepPoint**: The state of a particle (energy, momentum, position, etc.) immediately before a physical interaction or before crossing a geometric boundary.

   - **The PostStepPoint**: The state of the same particle immediately after a physical interaction or after crossing a geometric boundary.

   As the particle propagates through the system, its continuous trajectory is segmented into a discrete series of Steps defined by interactions or boundary crossings.

For this work, a custom-made Geant4 code of the Xenoscope TPC was developed, in which the geometry of the TPC was created, the physical parameters were set and the simulated particles were defined. In general, most of the code was already written, some modifications had to be performed. The code is saved in the following GitHub repository https://github.com/Physik-Institut-UZH/DemonstratorXenonscope. However, this repository is not publicly accessible at present. In this code the relevant simulation result data was defined and ordered to be stored in a ROOT [14] file, a specialised object oriented file structure designed for the requirements of particle physics. All simulations were executed on the high performance computing cluster in the farm environment of the Physics Department at the University of Zurich. Further data analysis was performed using the Python programming language, utilising standard scientific libraries including `NumPy`, `SciPy`, and `Matplotlib`, with `Uproot` employed to access the ROOT files.

4.2 Simulated Geometry of the Time Projection Chamber

The entire geometry of the Xenoscope TPC including all interior components, the liquid and gaseous xenon, was simulated in Geant4. This includes all material properties, on an atomic level, to account for microscopic interactions between the components of the TPC and generated primaries, which were photons for this study. It was necessary to create new code segments that define the geometry of the photosensors at the top. The array itself was implemented as an almost cylindrical volume on top of the active LXe. The specific geometry and arrangement of the SiPMs were not modelled directly in Geant4 instead, these parameters were implemented during the analysis. The positions and sizes of each SiPM were created according to the design of the actual photosensor array that is visualised in Figure 14. Photons arriving on the photosensor array were categorised depending on the specific point they would reach. Photons incident on the SiPMs were counted as a signal hit and photons which arrived outside, on the PTFE parts, were counted as non-detections.

The simulated geometry of the TPC can be visualised by creating a simulation of Geantino particles, a fictional particle that does not interact with matter, in all of the TPCs components. The distribution of these particles throughout all volume elements allowed the entire simulated TPC structure to be clearly visualised as seen in Figure 15a. The main structure consists of the cryostat shell, which is coloured in grey, the copper rings of the field cage in green, the polyamide-imide pillars that hold the copper rings at place in brown, the LXe in red and the GXe in yellow. The implementation of the LXe allowed for the distinction between the active and inactive LXe, as illustrated in Figure 15b. As mentioned in an earlier section, the photosensor array is on top of the active LXe which is inside the TPC field cage and the inactive LXe is located outside of it. However, it is still possible for photons generated in the inactive volume to reach a SiPM detector element. To distinguish the initial position of photons coming from the active or inactive LXe this differentiation was made.

To retrieve interaction data from the simulation, it was necessary to designate specific geometric regions as Sensitive Volumes. In Geant4, a Sensitive Volume is a logical volume configured to digitise particle interactions. This means that energy deposition and position data from events occurring within this volume among other information are extracted and stored in the ROOT file. For this work, the following volume types were set as Sensitive:

- Active liquid xenon
- Inactive liquid xenon
- Gaseous xenon
- Photosensor array

All other volume elements (copper rings, cryostat, etc.) were set as Passive Volumes in which interactions were not recorded. To construct the detector geometry, the physical properties of the materials were defined. Standard materials, including the copper for the field cage rings and the stainless steel for the cryostat, the PTFE for the photosensor cover, and polyamide-imide for the pillars, were created using the Geant4 NIST database [30] (via `G4NistManager`). The isotopic composition of the xenon was also taken from the NIST database, which defines the composition according to the natural abundance as previously shown in Table 1. All optical parameters of the used materials can be found in Table 2. The origin of reference is set at the bottom of the inner vessel in the centre of the active volume as seen in Figures 15a and 15b. The active surface of the photosensor array was located at height $z = 2912.77$ mm. The boundary between LXe and GXe was located at $z = 2793.74$ mm.

Material	Absorption coefficient	Reflection coefficient	
Polyamide-imide	0.90	0.10	
Steel	0.43	0.57	
PTFE	0.05	0.95	
Copper	0.80	0.20	
Material	**Refractive index**	**Rayleigh scattering length**	**Absorption length**
LXe	1.58	30 cm	100 cm
GXe	1.00	100 m	100 m

Table 2: Overview of the optical properties of the materials used in the simulated TPC.

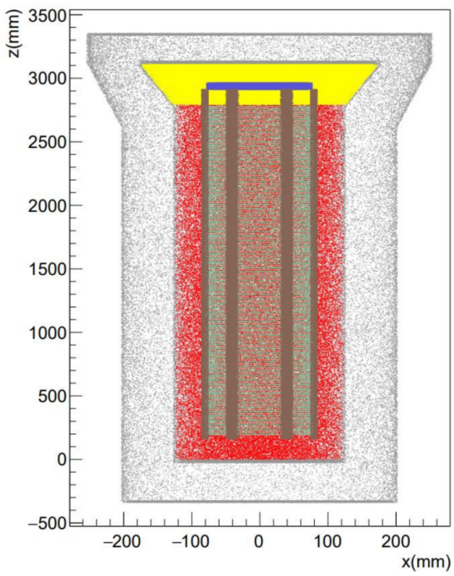

a)

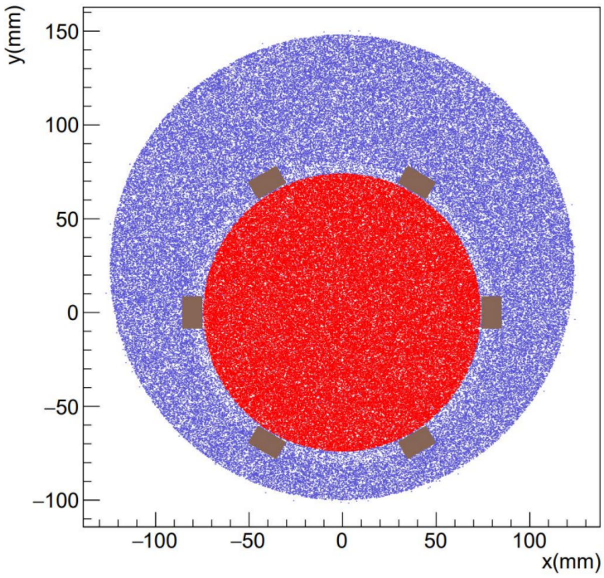

b)

Figure 15: *a) A Geantino simulation of the different components of the Xenoscope TPC. Grey: cryostat, yellow: gaseous xenon, red: liquid xenon, brown: polyamide-imide pillars, green: copper rings, blue: photosensor array. b) A simplified top view of the Geantino simulation. In red one can see the active LXe volume which is located inside the TPC field cage and directly below the SiPMs. In blue the inactive LXe volume is highlighted. The brown colour indicates the polyamide-imide pillars.*

4.3 Particle Generation

The Geant4 framework offers the user the ability to simulate all types of particles. The intrinsic properties such as mass, charge, spin, and lifetime are assigned to individual particles according to the PDG [25]. As briefly mentioned earlier, in Geant4 the initial generated particles are called the primaries, which can be distinguished from particles arising from interactions and decays. Before simulating any primaries, the following fundamental initial conditions were set:

- **Particle type:** `G4OpticalPhoton` [19] (low-energy photon)
- **Emission shape:** A thin circular disk at height z, spanning the full cross-sectional area of the inner vessel
- **Emission direction:** Isotropic
- **Energy:** 7eV (scintillation energy)
- **Confined volume element:** active and inactive LXe
- **Number of primaries:** 10^7

To closely replicate the scintillation photon of xenon, all primary particles were defined as photons and emitted isotropically at the xenon scintillation wave length of 175 nm which corresponds to a photon energy around 7 eV. To account for all possible event locations, the primary particles were generated on a circular disk at a defined height inside the active and inactive LXe. The amount of primaries generated was 10^7 in each simulation in order to obtain a sufficiently large sample size. As a reference, a muon crossing the Xenoscope TPC at a 30° angle with respect to the horizontal axis can generate approximately $2 \cdot 10^6$ photons. Therefore, the emitted number of photons represents a realistic amount that could be generated by an interaction. Once all conditions were set, Geant4 could simulate the passage of the defined particles through the volume elements recording the interaction and transport data.

4.4 The Physical Processes

The physical interactions which the created particles undergo are governed by the physics lists that are selected for the simulation. In these physics lists, all interaction properties and cross-sections are defined. Geant4 provides a vast collection of physics lists [21] which can be used to study physical processes. From these lists a selection has to be made, which fit the best for the intended study. It is also possible to use custom created physics lists or to modify existing lists for a specific problem. Although the primary focus of this study was mainly restricted to electromagnetic interactions, the Geant4 architecture requires the initialisation of a complete physics environment. Consequently, two physics lists were utilised to define the models governing electromagnetic and hadronic interactions.

For electromagnetic interactions the physics library Livermore electromagnetic physics [17] was chosen. The Livermore library is based on tabulated values obtained from EPDL97 [31] which is a maintained database of photon interactions which is the main reason why this library was chosen for this work. The Livermore library incorporates Doppler broadening for Compton scattering and utilises accurate atomic form factors to model Rayleigh scattering. Because Rayleigh scattering is the dominant interaction mechanism for 7 eV photons, precisely modelling this process is crucial for the results presented in this work. In order to be able to describe interactions on all energy ranges Livermore extrapolates the tabulated values to the broader energy regime which starts at 0 eV up to 100 TeV. A detailed overview is given in Table 3. In contrast, the standard electromagnetic physics library is based on analytical computed values for higher energy regimes which lose accuracy in lower energy regions. Although the Livermore library also loses accuracy in such a low energy regime (scintillation photon energy ≈ 7 eV) it suits the problem better since it is based on tabulated values. An overview over this library can be found in Table 8.

For the hadronic interactions the physics list `QGSP_BERT_HP` [18] was chosen. For high energy interactions Quark-Gluon String (QGS) model is applied to handle the initial projectile and nucleon collision, followed by a Precompound (P) model which manages the subsequent nuclear de-excitation. In intermediate energy range the Bertini Intra-Nuclear Cascade (BERT) model is utilised. The High Precision (HP) suffix denotes that a precise model for neutron interactions in the lower energy scale was employed. A detailed overview of this list can be found in Table 4.

Particle	**Interaction**	**Model Class**	**Range**	**Description**
Photons (γ)	Photoelectric	`G4LivermorePhotoElectric`	0 eV - 100 TeV	Models cross-section for atomic shell absorption edges.
	Compton	`G4LivermoreCompton`	0 eV - 100 TeV	Specialised model used to simulate the inelastic scattering of photons off electrons (includes Doppler-broadening).
	Rayleigh	`G4LivermoreRayleigh`	0 eV - 100 TeV	Models coherent scattering using atomic form factors, dominant at low energies.
	Pair Prod.	`G4LivermoreGammaConversion`	1.02 MeV - 100 TeV	Model for e^+e^- pair production.
Electrons (e^-)	Ionisation	`G4LivermoreIonisation`	10 eV - 100 GeV	Uses tabulated stopping powers for soft collisions.
	Bremsstrahlung	`G4LivermoreBremsstrahlung`	10 eV - 100 GeV	Data-driven model responsible for simulating braking radiation
Positrons (e^+)	All	Standard Models	all	Default analytical models are used (no specific Livermore data available).

Table 3: Detailed specifications of the electromagnetic models within the **Livermore** electromagnetic physics library, including their valid energy ranges and underlying algorithms. Content of this table obtained from [17].

Particle	**Energy Range**	**Model**	**Description**
Hadrons (p, π, K)	> 12 GeV	**QGS**	Quark-Gluon String model, handles high-energy string fragmentation.
	< 6 GeV	**Bertini**	Intranuclear Cascade model, simulates interactions with individual nucleons.
	3 - 25 GeV	**FTF**	The Fritiof parton model treats hadrons as bound states of partons (quarks and gluons) held together by a string of the strong force.
	0 - 100 TeV	**FTF**	The Fritiof parton model only for anti particles (anti-protons, anti-neutrons, ...)
Neutrons (n)	> 20 MeV	**Bertini / QGS**	Follows standard hadronic models.
	< 20 MeV	**NeutronHP**	High Precision data driven model, uses ENDF/B-VII libraries for exact resonances and capture.
EM $(e^{\pm}, \gamma)$	All Energies	**Standard EM**	standard electromagnetic interactions (not used in this work).

Table 4: Summary of the physics models utilised in the `QGSP_BERT_HP` physics list, categorised by particle type and energy regime. Content of this table is obtained from [18].

4.5 Goal of the Simulation

One of the main goals was to determine the LCE which serves as a fundamental performance parameter for a TPC. Physically, the LCE represents the total probability that a single scintillation photon will survive the transport process, navigating geometric losses, absorption in the medium, and surface reflections and trigger a signal in the photosensor array. A high Light Collection Efficiency is critical for rare event searches such as dark matter detection which aims to measure faint recoil signals. In addition, a high LCE is necessary to gain a better distinction between signal and noise.

In the case of the Xenoscope which does not have the purpose of detecting WIMPs but serves as an R&D setup, it is also necessary to fully understand its optical performance. For one, it is important to give a proof of concept that photons inside the TPC can indeed survive the entire length of 2.6 m, which is a driving factor for building larger next-generation detectors. Secondly, Xenoscope is also designed to drift electrons over its entire length, but the measured signal will be photons created in the electron avalanche at the LXe GXe interface. Without knowing the optical performance of the TPC there is no possibility to quantify the obtained signals. Furthermore, characterising the LCE enables the accurate measurement and quantification of background events induced by particles traversing the TPC and creating a categorisation of background created by different types of particles. These reasons make it essential that the optical performance of the Xenoscope TPC is fully understood.

The Light Collection Efficiency of the TPC is given as the following ratio:

$$LCE = \frac{N_{det}}{N_{gen}}, \tag{4}$$

where N_{det} is the number of photons that reach the photosensors and N_{gen} is the total number of photons initially generated inside the LXe. The factor N_{det} has a strong dependence on the initial height z at which the primaries were emitted. To investigate the effect of emission height on the LCE, several simulations with varying z were conducted.

In the past, another study was performed to analyse the LCE of an older version of the Xenoscope TPC in a simulated environment by Rachana Yajur [67]. In contrast to this study, their work did not include the real geometry of the physically constructed TPC which was not yet available at the time. The main difference is that the older version of the TPC also included an array of photomultiplier tubes at the bottom and additional SiPM rings around the field cage. Their result showed that the LCE depends on a sum of two exponential functions of the increasing height. In this thesis, the exact geometry of the physical TPC is studied for the LCE simulations. The obtained dependence will then be compared qualitatively with the previous work in order to see if the results agree.

5 Results

In order to obtain the relation between Light Collection Efficiency and vertical emission height z several simulations were performed and analysed. The Geant4 parameters have been set as discussed in previous Chapter, and the results obtained from these simulations are presented here. A simplified overview on how the simulations were configurised can be found in Figure 16.

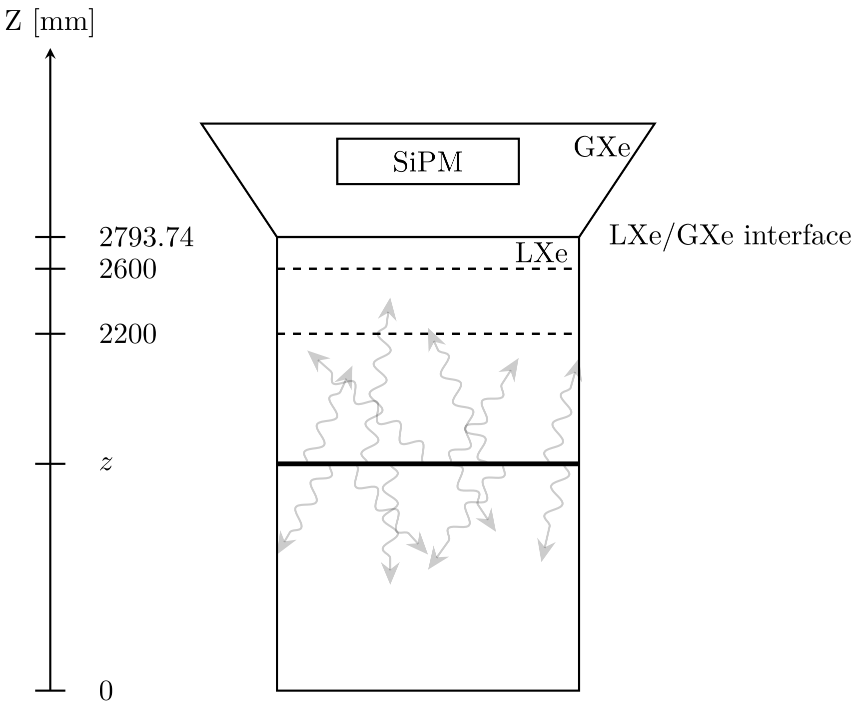

Figure 16: *A simplified visualisation on how the simulations were created. At a specific height z inside the LXe 10^7 photons (wavy arrows) were generated on the entire cross-sectional area and emitted in all directions inside the TPC . This procedure was repeated for different heights z. The position of the presented simulations performed at heights $z = 2200$ mm and $z = 2600$ mm with correct relative position to the LXe/GXe interface are marked with dashed lines. The third presented result at $z = 2793.73$ mm is located just below this interface.*

5.1 Light Collection Efficiency

The Geant4 simulation data allowed the analysis of the active coverage of the photosensor array. In doing so, it was possible to calculate the fraction of incident photons lost to the non-sensitive PTFE cover located between the individual SiPMs. To gain an estimate on the amount of lost photons, the data obtained from individual simulations was analysed. One example can be seen in Figure 17. Each photon reaching the top array is visualised either in red or in blue. A red point indicates a photon hit on a SiPM sensor, and a blue point indicates a photon that reached the PTFE cover of the array and missed the SiPMs. All blue coloured photons are therefore not detected. To obtain this figure, a simulation of 10^7 photons which were generated at $z = 2600$ mm, located around 194 mm below the interface between LXe and GXe, was performed (see Figure 16 for relative position). As briefly mentioned in Chapter 4 this number of emitted photons was chosen because real known interactions can create a similar amount of photons. In addition, to obtain statistical significance, it was necessary to create a high sample size. This specific value of z was chosen in order to provide enough data points to create a general statement. Another reason for this choice was that the figure should also contain some white spots such that it is clear that each coloured point really represents an individual photon. Two additional results for different choices of z can be found further on.

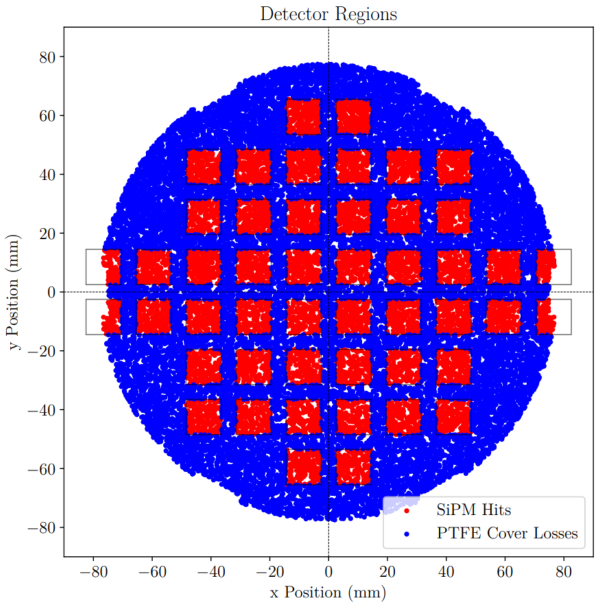

Figure 17: *Visualisation of incident photons on the top photosensor array. Red dots indicate hits on the active SiPM detector surfaces, while blue dots mark photons absorbed by the inactive PTFE cover. The vertical emission height was at* $z = 2600$ *mm.*

N_{gen}	10^7
N_{arr}	28170
N_{det}	9623
N_{loss}	18547
N_{arr}/N_{gen}	$2.82 \cdot 10^{-3}$
N_{det}/N_{arr}	0.341
N_{det}/N_{loss}	0.519
LCE $= N_{det}/N_{gen}$	$9.62 \cdot 10^{-4}$

Table 5: Data obtained from a simulation of photons emitted at initial height $z = 2600\,\text{mm}$.

The results seen in the Figure 17 are summarised in Table 5. N_{gen} is the total amount of primary photons generated, N_{det} is the number of red points which resemble photons reaching a SiPM element, and N_{loss} is the number of blue points that describe photons reaching the PTFE cover, N_{arr} is the total number of photons that reach the photosensor array which is the sum of all the red and blue points. The number of total photons that reach the top array is found to be 28170, which is $\approx 2.8\%$ of the total number of photons. Of these, 9623 photons reach a SiPM detector which brings the number of detected photons to $\approx 34\%$ of all photons reaching the top array. So around a third of all photons reaching the top array are detected. Compared to the total number of photons generated, these make up only $\approx 0.09\%$. This value is the LCE for this specific emission height $z = 2600\,\text{mm}$.

Repeating this procedure for different initial emission heights and computing the LCE for each individual z gives us the trend seen in Figure 18a. The individual step sizes in z were chosen according to how the LCE evolves. In regions where the curve does not change much, a larger step size was chosen and, in regions where the growth is the strongest, smaller step sizes were taken to obtain a better granularity. The individual simulation data are not presented here, but are also stored on the farm computer environment of the University of Zurich. A total of 17 simulations were created to obtain this figure.

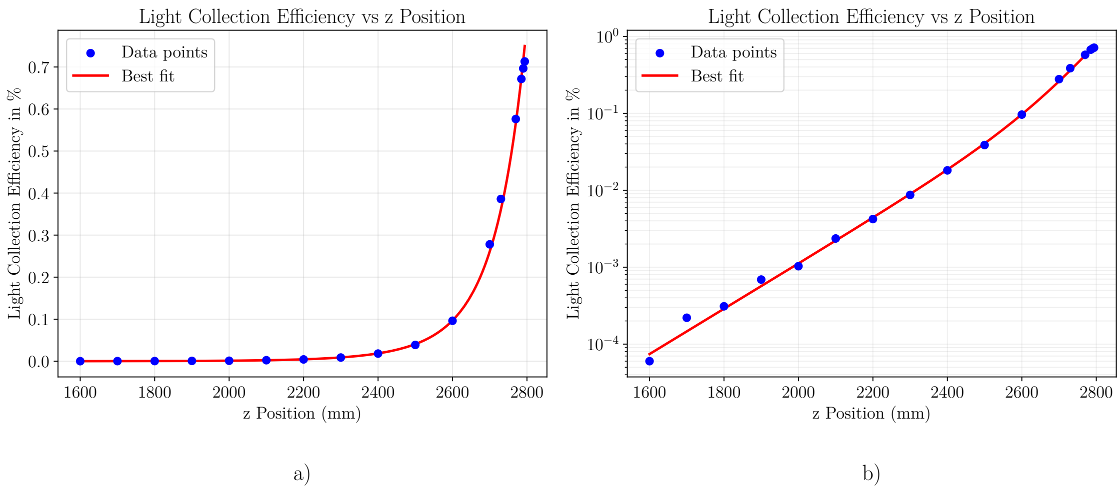

Figure 18: *From several simulations where primaries are generated at different z, the following relation between the LCE and z is obtained. a) Simulated LCE data fitted with a sum of two exponential functions. b) The same data and fit presented on a logarithmic scale.*

It is clearly visible that the LCE increases with increasing height z or decreasing depth of the initial emission position of the primaries that were generated. Since the photosensor array is placed at the top of the GXe, primaries emitted at a higher location are closer to the SiPMs. This proximity increases the likelihood that they will be successfully detected. At values of $z = 2000\,\text{mm}$ and below the LCE drops to $\approx 0\%$. For photons generated at this height and below almost no detection is expected. The fit reveals that the LCE depends on a sum of two exponential functions of height z, in good agreement with results obtained from a prior Master thesis by Rachana Yajur [67]. The maximum value of the LCE is $\approx 0.71\%$ and is given at $z = 2793.73\,\text{mm}$, which is just below the interface between LXe and GXe.

To verify the exponential nature of the growth, a logarithmic plot is presented in Figure 18b. In the logarithmic plot it is clearly visible that the best fit line follows very closely the obtained data points, which indicates that the fit is in a very good agreement with the data. The following relation for the LCE in dependence of z can be extracted from the parameters of the best fit line:

$$LCE(z) = 7.4 \cdot 10^{-7} \cdot e^{6.8 \cdot 10^{-3} \cdot z} + 2.2 \cdot 10^{-10} \cdot e^{1.4 \cdot 10^{-2} \cdot z} \quad (5)$$

One can see that the first exponential is much less suppressed with a constant pre-factor proportional to 10^{-7}, while the second exponential has a greater suppression with a pre-factor in the order of 10^{-10}. The pre-factors have a greater impact on lower values of z, since on higher values the exponential parts will dominate more. The factors $6.8 \cdot 10^{-3}$ and $1.4 \cdot 10^{-2}$ in the exponents describe the attenuation of the photons propagating in the TPC. The lower these numbers are, the more photons cannot reach the photosensors due to various effects such as the geometry of the setup and the material properties of xenon. A geometric influence on these parameters is that there are no reflectors along the walls of the inner vessel or along the inside and outside of the field cage. According to Table 2 the reflectivity of the stainless steel inner vessel is around 60%, meaning only this fraction of photons that reach the walls of the outer vessel are redirected towards the inner parts. The reflectivity of the copper rings are even worse with only 20%, absorbing most of the photons that reach them.

5.2 Deflection Angles of Detected Photons

In a second part, the analysis of deflection angles of detected photons was performed. In spherical coordinates, the emission direction of a photon has a contribution to the azimuthal direction ($\varphi_{initial}$) and the polar direction ($\theta_{initial}$), which can be extracted from Geant4. A detected photon has an initial starting position and a final detection position on the SiPM in 3D space. The vector connecting these two points can be decomposed in a contribution in φ_{det} direction but more importantly in θ_{det} direction which is the angle between initial emission direction to the z-axis. By comparing the polar angles between emission direction and detection direction of a photon, one can find its net deflection angle. This angular shift is the cumulative result of Rayleigh scattering within the LXe and reflections off internal detector components as detailed in Table 2 during propagation. The angle of deflection is therefore given as:

$$\theta_{defl} = \theta_{det} - \theta_{initial} \tag{6}$$

Note that Equation 6 only gives information about the net deflection angle projected towards the z-direction, whereas in general there could be many scattering processes involved in all kinds of directions during the propagation time of a photon in the xenon.

The simulation data created in the Light Collection Efficiency simulations was reused to analyse the deflection angles. To be consistent with the previous results, the same height $z = 2600$ mm was chosen. Figure 19a presents a histogram detailing the photon count per bin as a function of the deflection angle.

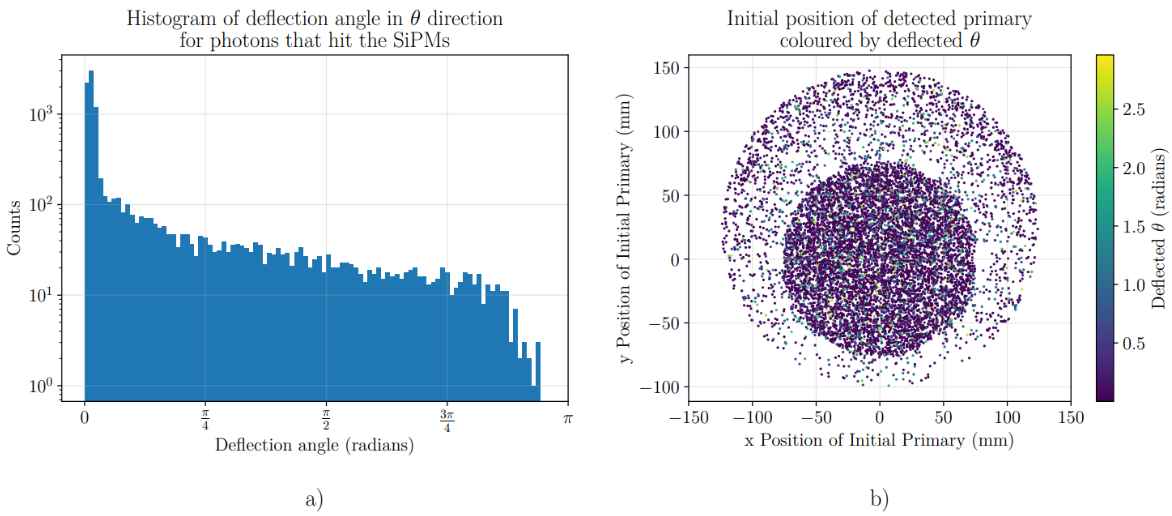

Figure 19: *Graphical representation of deflection angles for a simulation where primaries were generated at $z = 2600$ mm. a) Histogram of deflected photon angles in θ direction in logarithmic scale. b) Initial positions of primary photons that reach a SiPM detector. Individual primaries are coloured by the deflected angle in θ direction.*

Another study that can be performed is by plotting the initial position of the primary photon before emission in the x-y plane and colour coding it according to the net angle of deflection. Consequently, Figure 19b is obtained. One can see that the dominant deflection angle θ_{defl} is around 0 radians which indicates that most of the photons were not deflected from their initial emission direction. Also notable is that many more photons arrive from the active LXe. The TPC field cage is located between the inactive and active LXe and consists of copper rings that according to Table 2 easily absorb 80% of the photons that reach it. It is reasonable to expect that more photons from the active region manage to reach the detectors.

A further quantity to analyse deflection angles is given by the deviation distance d between where the particle would have landed on the photosensor array plane if it had moved in a straight line (no scattering) and where it actually landed (real trajectory). This distance d is given according to the following equation:

$$d = \sqrt{(x_{det} - x_{proj})^2 + (y_{det} - y_{proj})^2} \tag{7}$$

where x_{det} and y_{det} define the detected x-y positions of the particle on the detector, x_{proj} and y_{proj} are the projected x-y positions onto the detector plane if the particle would not have scattered and followed its initial emission direction. Note that the z position of the SiPM array and the vertical emission height are both fixed.

In Figure 20a the resulting histogram of the deviation distance d is presented. Most of the photons are contained in the bins close to zero deviation, which confirms that these photons reached a SiPM element without being significantly altered from their initial emission direction. This is in good agreement with the results obtained from analysing scattering angles. In Figure 20b this deviation distance d is plotted against the deflection angle θ_{defl}. In this distribution, one can see that with an increasing deflection angle the deviation distance increases, which is the expected behaviour, since a greater angular deflection will automatically lead to a longer distance between the detection and projected point on the detector plane. The visible boundary at $\frac{\pi}{2}$ marks the limit where the initial photon emission direction stops pointing towards the detector. Any angle exceeding this threshold results in a trajectory that never intersects the detector plane. Also visible in this plot is that many points are located close to the origin giving a further confirmation to the prior obtained result that most photons that reached a detector element are not scattered significantly.

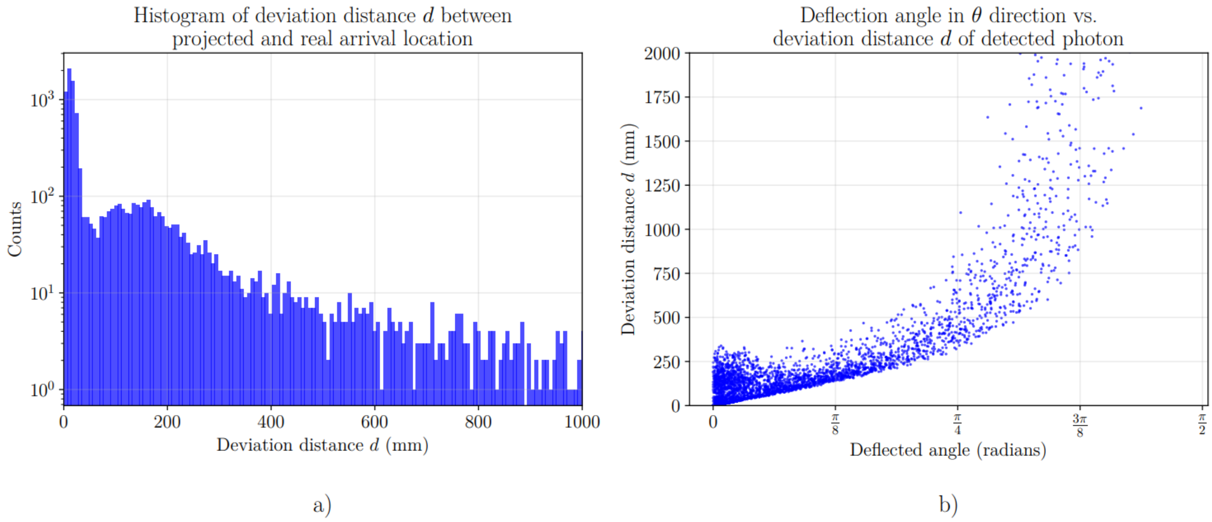

Figure 20: *Graphical representation of deviation distance d and comparison to deflection angle θ for a simulation with* 10^7 *photons initially emitted at z = 2600 mm. a) Histogram of deviation distance d in logarithmic scale. b) Deflection angle θ vs deviation distance d.*

5.3 Additional Results

The presented results above were specifically chosen examples to create a fundamental understanding. To extend these, two edge case results are presented here for two additional values of z. The first, at $z = 2200\,\text{mm}$, yields very few photons reaching the SiPM array, leading to overall lower counts. The second, at $z = 2793.73\,\text{mm}$, is located within the LXe but immediately below the GXe boundary. This second height produces a very high number of detected photons and overall higher counts.

5.3.1 Light Collection Efficiency

In the case of $z = 2200\,\text{mm}$ a similar approach was made as presented above. The obtained values and ratios can be extracted from Table 6 and a visualisation can be found in Figure 21. The ratio between red dots and blue dots remains the same with approximately 34%. The LCE in this case is given as $\approx 0.004\%$.

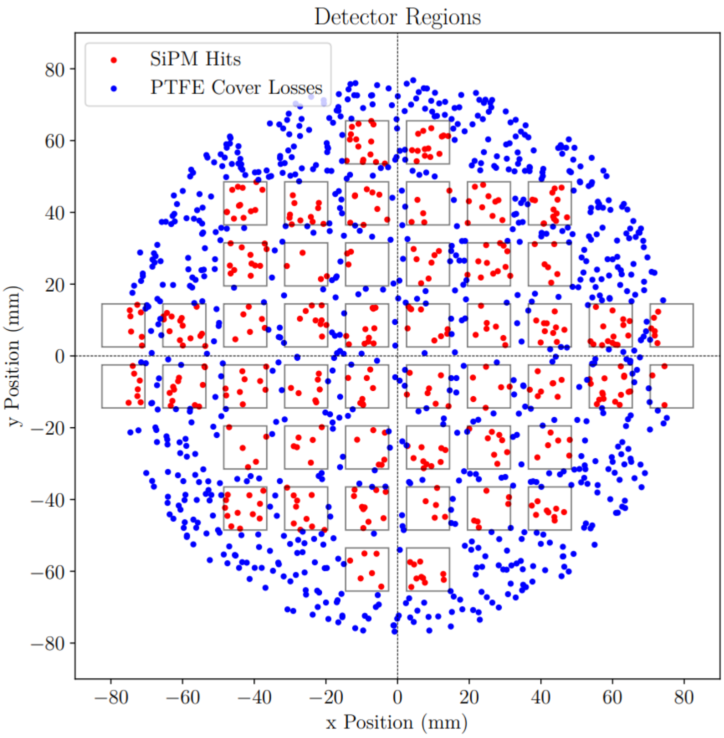

Figure 21: *Visualisation of incident photons at the top photosensor array. Red dots represent photons striking the active SiPM surfaces, while blue dots indicate photons landing in the passive gaps between sensors. The initial emission depth was set to* $z = 2200$ *mm.*

N_{gen}	10^7
N_{arr}	1237
N_{det}	422
N_{loss}	815
N_{arr}/N_{gen}	$1.23 \cdot 10^{-4}$
N_{det}/N_{arr}	0.341
N_{det}/N_{loss}	0.518
LCE $= N_{det}/N_{gen}$	$4.22 \cdot 10^{-5}$

Table 6: Data obtained from a simulation of photons emitted at initial height $z = 2200$ mm.

In the other case where the height was chosen as $z = 2793.73$ mm the obtained values and ratios can be extracted from Table 7 and a visualisation can be found in Figure 22. The ratio between red dots and blue dots is slightly higher with approximately 36%, which matches precisely the SiPM coverege of the photosensor array. The LCE in this case is given as $\approx 0.71\%$.

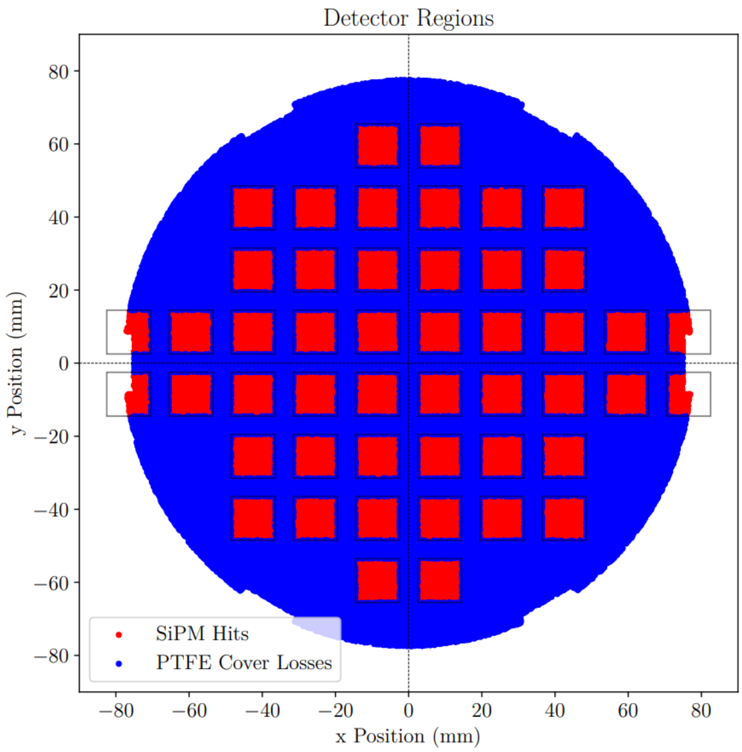

Figure 22: *Visualisation of incident photons at the top photosensor array. Red dots represent photons striking the active SiPM surfaces, while blue dots indicate photons landing in the passive gaps between sensors. The initial emission depth was set to* $z = 2793.73$ *mm.*

N_{gen}	10^7
N_{arr}	196246
N_{det}	71321
N_{loss}	124925
N_{arr}/N_{gen}	0.0196
N_{det}/N_{arr}	0.363
N_{det}/N_{loss}	0.571
LCE $= N_{det}/N_{gen}$	0.0071

Table 7: Data obtained from a simulation of photons emitted at initial height $z = 2793.73$ mm.

5.3.2 Deflection Angles of Detected Photons

Observing the deflection angles given from Figures 23a and 24a one can see similar to the discussion from earlier that most of the detected photons were not deflected from their initial emission direction.

Investigating the colouring in Figures 23b and especially 24b confirm that the deflection angles are located around zero. In addition, in Figure 24b one can see in the white spots the positions of the polyamide-imide pillars which were not visible in Figure 19b.

Furthermore, it is also possible to analyse the deviation distance d for the additional emission heights presented here. In doing so, one obtains the two histograms in Figures 25a and 26a.

Note that in Figure 25a the y-axis is not in logarithmic scale, since the photon count is not high enough. In Figures 25b and 26b the deflection angle θ is plotted against the deviating distance d. The trend is the same as discussed above, the distance d grows if the deflection angle increases. A big collection of points can be found close to the origin indicating that a lot of photons did not scatter much if they reached a SiPM element.

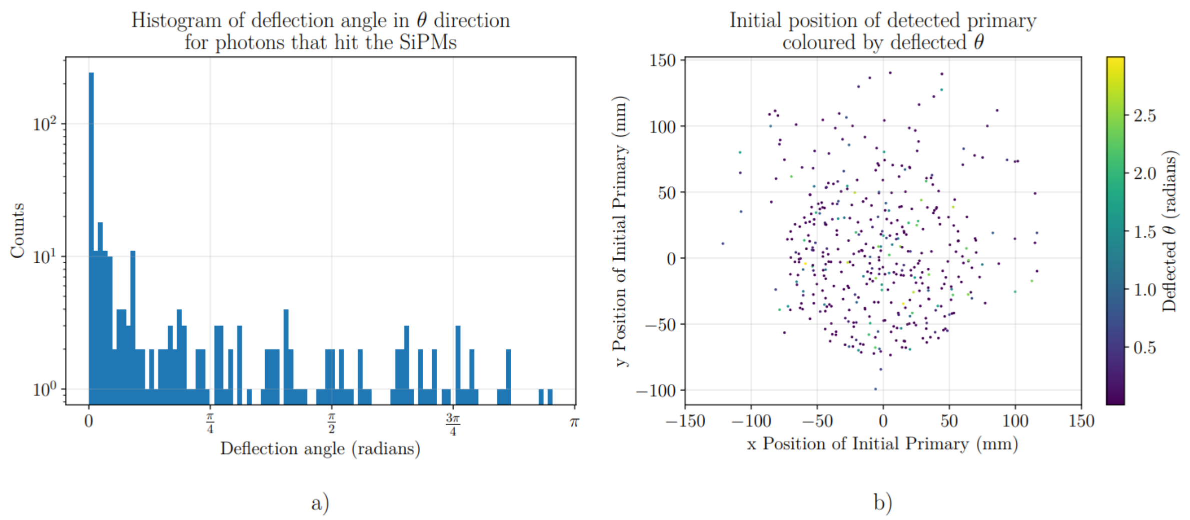

Figure 23: *Graphical representation of deflection angles for a simulation where primaries were generated at $z = 2200$ mm. a) Histogram of deflected photon angles in θ direction in logarithmic scale. b) Initial positions of primary photons that reach a SiPM detector. Individual primaries are coloured by the deflected angle in θ direction.*

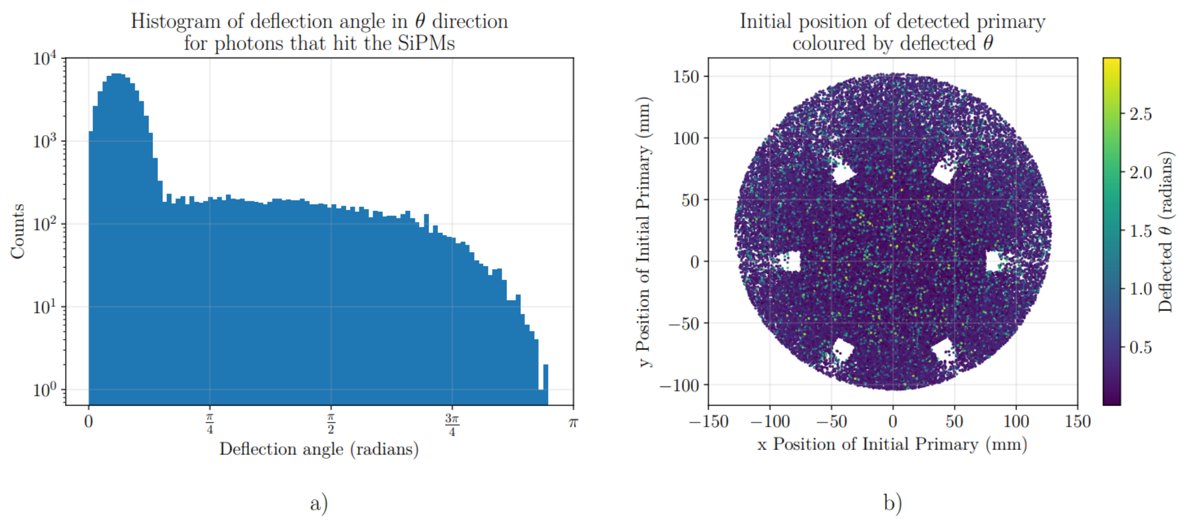

Figure 24: *Graphical representation of deflection angles for a simulation where primaries were generated at $z = 2793.73$ mm. a) Histogram of deflected photon angles in θ direction in logarithmic scale. b) Initial positions of primary photons that reach a SiPM detector. Individual primaries are coloured by the deflected angle in θ direction.*

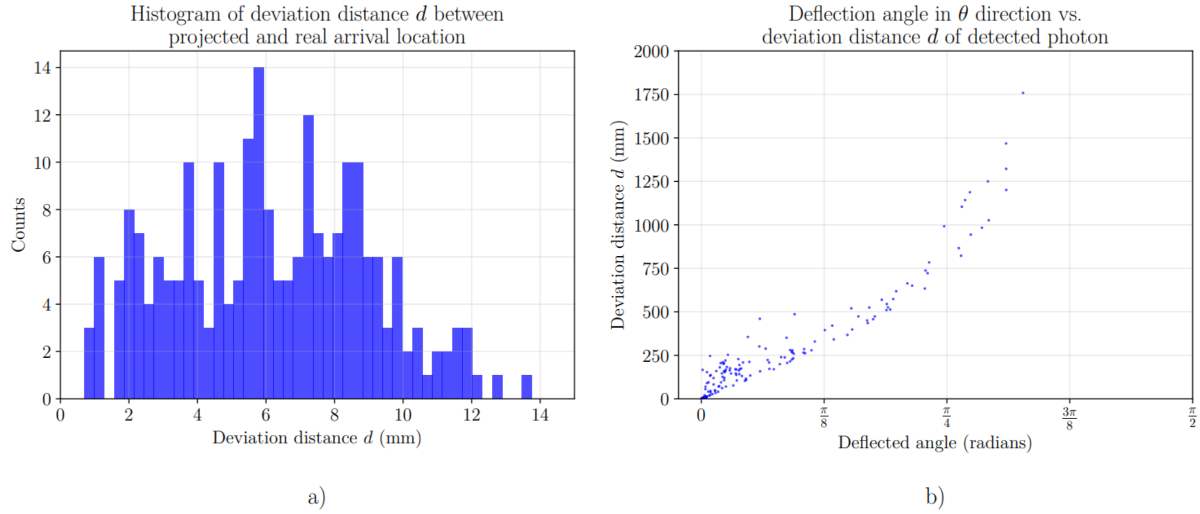

Figure 25: *Graphical representation of deviation distance d and comparison to deflection angle θ for a simulation with* 10^7 *photons initially emitted at z = 2200 mm. a) Histogram of deviation distance d. Note scale is not logarithmic. b) Deflection angle θ plotted against deviation distance d.*

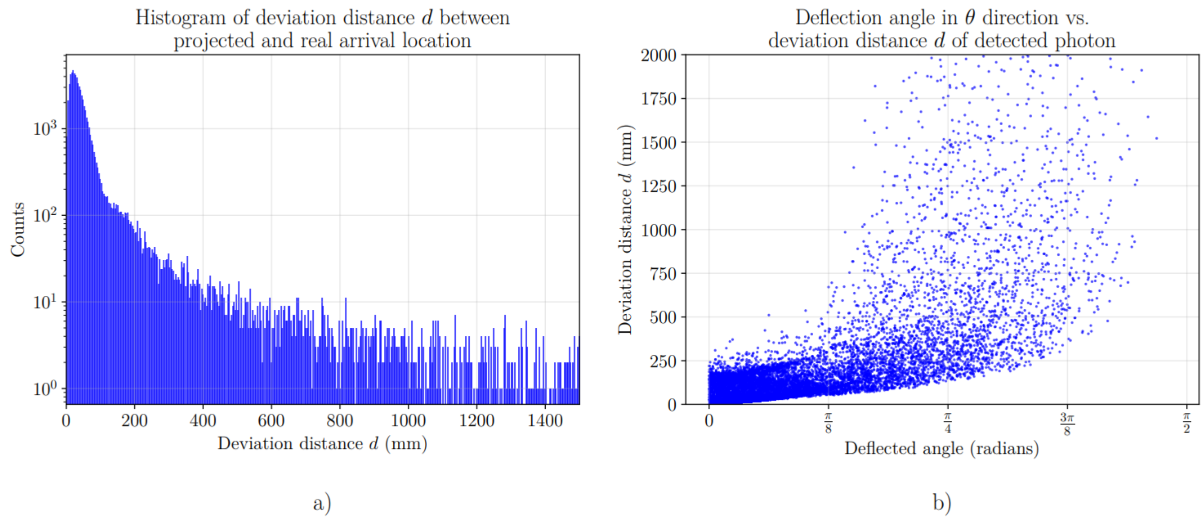

Figure 26: *Graphical representation of deviation distance d and comparison to deflection angle θ for a simulation with* 10^7 *photons initially emitted at z = 2793.73 mm. a) Histogram of deviation distance d in logarithmic scale. b) Deflection angle θ plotted against the deviation distance d.*

5.4 Consistencies of the Simulations

To verify the correctness of the simulations, some effects that could have impact on the results were analysed. One of these verifications was done by studying whether some photons could be counted several times. Ideally, a photon reaching the SiPM is absorbed after detection. However, it is possible for the photon to scatter off the detector surface back into the GXe volume after being counted as a signal. If this photon undergoes further scattering and returns to the SiPM, it could be counted a second time. This way it would be possible that a single photon would be counted as two different photons which could influence the obtained results.

A different validation of the simulations was done by investigating whether unexpected interactions within the xenon could generate additional photons again altering the results. This validation was done by observing whether a photon had a ”parent” or not. Particles generated through primary interactions originate from a specific parent particle. This relationship is explicitly preserved within the Geant4 tracking system, storing the information whether a particle is created in secondary processes. If secondary created photons were present within the volumes obtained from unexpected interactions they could create additional signals on the SiPMs which would influence the results.

In general, these inconsistencies were ruled out as a contributor to result altering effects for the simulations. As these verifications serve primarily as methodological validation rather than experimental results, the more extended discussion of the precise procedure can be found in the Appendix.

6 Conclusion and Outlook

In this study, the Light Collection Efficiency of the Xenoscope TPC was characterised using Geant4 simulations. The reliability of the simulation was established by verifying that photon hits were correctly stored in the ROOT files and confirming that no significant secondary photons were generated by unconsidered interactions within the xenon. The presented result observed that only approximately 34% of the photons that reach the top array could be detected. This result agrees with the area coverage of the array surface with SiPMs which was 36%. This value is even better approached by a simulation created very close to the GXe boundary.

Secondly, the LCE was computed in dependence on the event depth and it was observed that the LCE exponentially declines with increasing depth. In other words, the LCE increases with increasing height z and reaches its maximum at the interface between LXe and GXe. This exponential trend was verified using logarithmic plotting and is in good agreement with the theoretical expectations and previous results reported by Rachana Yajur [67]. Using a best fit line on the data points, it was possible to extract the precise function that describes the behaviour of the LCE in dependence of z, which was a sum of two exponential functions. The obtained function suppressed the LCE in the lower regions of the TPC due to very low pre-factors causing a very low LCE in that region. In the upper regions of the TPC close to the LXe/ GXe interface the exponential parts started to dominate which would allow the LCE to rise. Since there are no reflectors employed in the TPC, photons that reach a wall or the field cage are often absorbed, which creates low attenuation coefficients. The overall efficiency is even more limited by the active area of the top array as stated above.

The analysis of the deflection angles showed that the vast majority of the photons that reach the top array do not scatter significantly inside the xenon. It was therefore possible to conclude that photons with initial emission direction towards the SiPM array have a higher likelihood to be detected. Furthermore, the inactive LXe is outside of the TPC field cage and most photons emitted from there have to penetrate the copper rings to reach the SiPMs. This means that photons generated inside the active volume have better chances to reach the top array, whereas the photons from the outer volume can be easier absorbed. From this study no additional knowledge on the deflection angles for the photons that did not reach the detectors was gained.

Future data gathered by a real Xenoscope TPC run will allow a direct comparison with the simulation results obtained in this thesis. From observing discrepancies and consistencies with real data, one can study the underlying physics in more detail and use the obtained knowledge to tune the simulation framework such that it agrees with a real run. Moreover, future work could build upon and extend the findings presented in this thesis. For instance, the performance of the SiPMs was not included in this study. The addition of precise optical properties of the SiPM surfaces could impact the results on the LCE. In this study, the initial photon source was modelled as a circular disk with isotropic emission. Future studies could investigate the impact of varying the spatial distribution of the initial photon location and emission direction. In addition, the xenon was assumed to have no contamination, which in reality is not the case. Future investigations could involve the analysis of the expected impurities of the xenon and the influence these could have on the obtained results.

Lastly, the results presented here can inform the development of future detectors. For one, to mitigate the photon loss caused by the dead space between sensors, future studies could focus on optimising the area covered by the SiPMs on the photosensor array. Other improvements on the LCE include the addition of reflecting elements along the TPC wall to recover lost photons. The addition of more sensors on the bottom of the TPC could also increase the light gathered and further increase the value of the LCE.

7 Appendix

7.1 Standard Electromagnetic Interaction Physics Library

The specification of the electromagnetic model of the `G4EmStandardPhysics` can be found here as a comparison to the Livermore Electromagnetic physics library from Table 3.

Particle	Interaction	Model Class	Description
Photons (γ)	Photoelectric	`G4PEEffectFluoModel`	Analytical cross-sections based on atomic shell parameterisations.
	Compton	`G4KleinNishinaCompton`	Simulates scattering off free electrons (no Doppler broadening).
	Rayleigh	`G4RayleighScattering`	Analytical formulation for coherent scattering.
	Pair Prod.	`G4BetheHeitlerModel`	Describes the pair production process with corrections.
Electrons (e^-)	Ionisation	`G4MollerBhabhaModel`	Møller scattering for e^-e^- interactions and Bethe-Bloch energy loss.
	Brems.	`G4eBremsstrahlungRel`	Relativistic model; often coupled with Seltzer-Berger tables for low energies.
	Scattering	`G4UrbanMscModel`	Multiple Scattering algorithm to simulate deflection steps.
Positrons (e^+)	Annihilation	`G4eplusAnnihilation`	Simulates annihilation into 2γ.
	Ionisation	`G4MollerBhabhaModel`	Bhabha scattering for e^+e^- interactions.

Table 8: Summary of the electromagnetic models defined in the **Standard** Electromagnetic physics library `G4EmStandardPhysics`. These models rely primarily on analytical parameterisations covering the energy range from 0 to 100 TeV. Content of table obtained from [16].

7.2 Verification of Simulation Data

Unexpected and strange occurrences within the TPC were observed because if present these could have a significant impact on the results. As discussed before, the first part was done by observing if any photons inside the TPC could be created by strange interactions. If such photons would exist the Geant4 simulation would distinguish them from the initial emitted photons. The difference between these particles would be that the initial emitted primary photons do not have a "parent" since they are the first generation of particle that were generated inside the TPC. A photon created in an interaction would therefore have a parent. From the ROOT files, it is possible to extract the information about every particle whether it possess a parent or not. This information is stored in a parameter called the ParentID which is just an integer. A histogram of the ParentID is shown in Figure 27. One can see that no secondary particle (ParentID 1 or higher) was created in the simulation, which means all observed photons were indeed the primary generated photons.

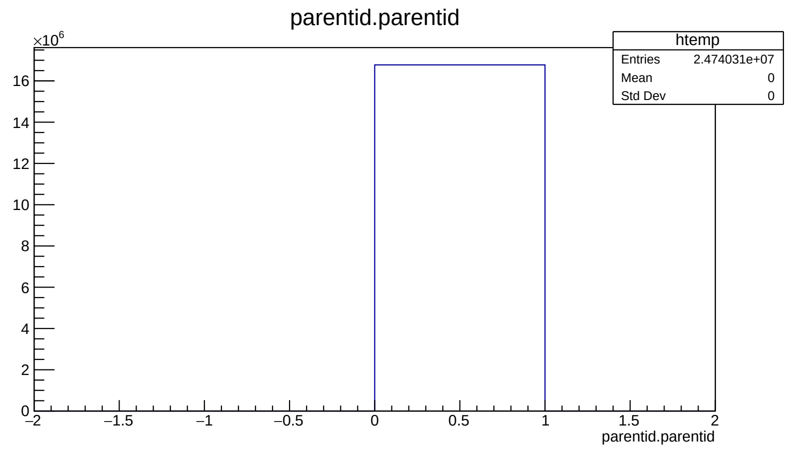

Figure 27: *From the ROOT file one can extract the information about whether a particle has a parent. All entries are located in the bin containing ParentID value 0.*

The next part was to check whether photons could be detected several times. As briefly mentioned before a photon can be double counted if it scatters on the SiPM and is redirected into the GXe/LXe in which it scatters again changing its trajectory again such that it reaches a SiPM for a second (or more) time. From the ROOT file the total amount of photons counted N_{count} and the number of photons that reached the photosensor array N_{arr} were extracted. This data leads to Table 9. One finds that around 0.1% of the photons can scatter back from the top array and be redirected towards it for at least one time. Since the entire photosensor array was considered and not only the SiPMs the influence of this effect on the signal is even more suppressed. From earlier results it was obtained that around 34% of the photons reaching the top array would be detected on a SiPM. Using this value, it is possible to reduce the percentage of photons that can reach a SiPM twice to around 0.034%. Furthermore, as mentioned in Chapter 4 the top array was implemented as PTFE only which has a high reflection coefficient according to Table 2. If one were to implement the SiPM parts as silicon, the reflectivity would be even lower. It is therefore possible to conclude that the influence of several counted photons is so small that it can be neglected.

N_{count}	28203
N_{arr}	28170
ΔN	33
$\Delta N/N_{arr}$	0.001

Table 9: The amount of total counts when a photon reaches the top array is compared to the number of individual photons that arrive at the top array. Data extracted from a photon simulation with primary emission at $z = 2600\,\text{mm}$.

References

[1] H. Acharya et al. Sterile-neutrino search based on 259 days of KATRIN data. *Nature*, 648(8092):70–75, 2025. arXiv:2503.18667, doi:10.1038/s41586-025-09739-9.

[2] M. Adrover et al. Commissioning of the 2.6 m tall two-phase xenon time projection chamber of Xenoscope. *JINST*, 20(04):P04013, 2025. arXiv:2411.08022, doi:10.1088/1748-0221/20/04/P04013.

[3] S. Agostinelli et al. Geant4—a simulation toolkit. *Nucl. Instrum. Meth. A*, 506(3):250–303, 2003. doi:10.1016/S0168-9002(03)01368-8.

[4] C. Alcock et al. The macho project: Microlensing results from 5.7 years of large magellanic cloud observations. *Astrophys. J.*, 542(1):281–307, October 2000. doi:10.1086/309512.

[5] R. Ansari. Eros: a galactic microlensing odyssey, 2004. URL: https://arxiv.org/abs/astro-ph/0407583, arXiv:astro-ph/0407583.

[6] E. Aprile and T. Doke. Liquid xenon detectors for particle physics and astrophysics. *Rev. Mod. Phys.*, 82(3):2053–2097, July 2010. doi:10.1103/revmodphys.82.2053.

[7] E. Aprile et al. The XENON100 dark matter experiment. *Astropart. Phys.*, 35(9):573–590, April 2012. doi:10.1016/j.astropartphys.2012.01.003.

[8] E. Aprile et al. The XENON1T dark matter experiment. *Eur. Phys. J. C*, 77(12), December 2017. doi:10.1140/epjc/s10052-017-5326-3.

[9] L. Baudis. Dual-phase xenon time projection chambers for rare-event searches. *Phil. Trans. Roy. Soc. Lond. A*, 382(2266), feb 2024. doi:10.1098/rsta.2023.0083.

[10] L. Baudis et al. Design and construction of Xenoscope — a full-scale vertical demonstrator for the DARWIN observatory. *JINST*, 16(08):P08052, August 2021. doi:10.1088/1748-0221/16/08/p08052.

[11] C. L. Bennett et al. First-year wilkinson microwave anisotropy probe (wmap)* observations: Preliminary maps and basic results. *Astrophys. J. Suppl.*, 148(1):1, sep 2003. doi:10.1086/377253.

[12] A. Bismark. Tests of the fundamentals of quantum mechanics with low-background experiments and detector technologies for liquid xenon time projection chambers. PhD thesis, University of Zurich, 2024.

[13] G. R. Blumenthal, S. M. Faber, J. R. Primack, and M. J. Rees. Formation of galaxies and large-scale structure with cold dark matter. *Nature Phys.*, 311(5986):517–525. doi:10.1038/311517a0.

[14] R. Brun and F. Rademakers. ROOT: An object oriented data analysis framework. *Nucl. Instrum. Meth. A*, 389:81–86, 1997. doi:10.1016/S0168-9002(97)00048-X.

[15] M. Carena, C. P. Burgess, J. S. Sekaric, et al. Review of particle physics: Dark matter. *Phys. Rev. D*, 112:010001, 2025. doi:10.1103/PhysRevD.112.010001.

[16] CERN. Electromagnetic physics constructors. Accessed: Januray 2026. URL: https://geant4.web.cern.ch/documentation/dev/plg_html/PhysicsListGuide/electromagnetic/emphyslist.html.

[17] CERN. Low energy electromagnetic physics - livermore. Accessed: January 2026. URL: https://geant4-internal.web.cern.ch/node/1619.

[18] CERN. Reference physics lists: Qgsp_bert. Accessed: Januray 2026. URL: https://geant4.web.cern.ch/documentation/dev/plg_html/PhysicsListGuide/reference_PL/QGSP_BERT.html.

[19] CERN. Geant4 physics reference manual – section: Optical photons, 2024. Accessed: February 2026. URL: https://geant4-userdoc.web.cern.ch/UsersGuides/PhysicsReferenceManual/html/electromagnetic/optical_photons/index.html.

[20] CERN. Geant4 collaboration website. https://geant4.web.cern.ch/, 2026. Accessed: January 2026.

[21] CERN. Geant4 physics list guide. https://geant4.web.cern.ch/documentation/dev/plg_html/PhysicsListGuide/physicslistguide.html, 2026. Accessed: January 2026.

[22] S. Chang, R. Edezhath, J. Hutchinson, and M. Luty. Effective wimps. *Phys. Rev. D*, 89(1), January 2014. doi:10.1103/physrevd.89.015011.

[23] LZ Collaboration. The lz dark matter experiment. *J. Phys. Conf. Ser.*, 718(4):042039, may 2016. doi:10.1088/1742-6596/718/4/042039.

[24] PandaX Collaboration. Dark matter search results from the pandax-4t commissioning run. *Phys. Rev. Lett.*, 127(26), December 2021. doi:10.1103/physrevlett.127.261802.

[25] PDG Collaboration. Review of Particle Physics. *Phys. Rev. D*, 110:030001, 2024. doi:10.1103/PhysRevD.110.030001.

[26] Planck Collaboration. Planck 2013 results. I. overview of products and scientific results. *Astron. Astrophys.*, 571:A1, 2014. doi:10.1051/0004-6361/201321529.

[27] Planck Collaboration. Planck2018 results: VI. cosmological parameters. *Astron. Astrophys.*, 641:A6, September 2020. doi:10.1051/0004-6361/201833910.

[28] XENON Collaboration. The XENONnT dark matter experiment. *The Eur. Phys. J. C*, 84(8), August 2024. doi:10.1140/epjc/s10052-024-12982-5.

[29] Xenoscope Collaboration. SiPM array of Xenoscope, a full-scale DARWIN vertical demonstrator. *JINST*, 18(03):C03027, March 2023. doi:10.1088/1748-0221/18/03/c03027.

[30] J. S. Coursey, D. J. Schwab, J. J. Tsai, and R. A. Dragoset. Atomic Weights and Isotopic Compositions (version 4.1), 2015. Available online: http://physics.nist.gov/Comp [2026-02-01]. URL: http://physics.nist.gov/Comp.

[31] D. E. Cullen, J. H. Hubbell, and L. Kissel. Epdl97: the evaluated photo data library '97 version. Technical report, Lawrence Livermore National Lab., CA (United States), 09 1997. URL: https://www.osti.gov/biblio/295438, doi:10.2172/295438.

[32] ESO. Comparison of rotating disc galaxies in the distant universe and the present day. ESO Image eso1709b, 2017. Accessed: April 2026. URL: https://www.eso.org/public/images/eso1709b/.

[33] ESO, ALMA, NRAO, and NAOJ, L. Calçada, Y. Hezaveh, et al. Gravitational lensing of distant star-forming galaxies (schematic). ESO Public Image: ESO1313b. https://www.eso.org/public/images/eso1313b/, March 2013. Accessed October 2025.

[34] ESO/L. Calçada. Artist's impression of the expected dark matter distribution around the milky way. https://www.eso.org/public/images/eso1217a/, 2012. Accessed: February 2026.

[35] L. Evans and P. Bryant. Lhc machine. *JINST*, 3(08):S08001, aug 2008. doi:10.1088/1748-0221/3/08/S08001.

[36] C. Ghag. The LUX direct dark matter search experiment. In *Interplay between Particle and Astroparticle physics*, 12 2014. arXiv:1412.4660.

[37] Google. Gemini [large language model], 2026. Accessed: April 2026. Usage Declaration: This AI assistant was used for light text editing, spell-checking, and suggesting alternative phrasing in accordance with UZH Physik-Institut guidelines. The author carefully verified all resulting text and takes full responsibility for its correctness. URL: https://gemini.google.com.

[38] K. Griest. The search for the dark matter: WIMPs and MACHOs. *Annals N. Y. Acad. Sci.*, 688(1):390–407, June 1993. doi:10.1111/j.1749-6632.1993.tb43912.x.

[39] F. Iocco, M. Pato, and G. Bertone. Evidence for dark matter in the inner milky way. *Nature Phys.*, 11(3):245–248, February 2015. doi:10.1038/nphys3237.

[40] J. E. Kim and G. Carosi. Axions and the strong CP problem. *Rev. Mod. Phys.*, 82(1):557–602, 2010. arXiv:0807.3125, doi:10.1103/RevModPhys.82.557.

[41] A. Kusenko. Sterile neutrinos: The dark side of the light fermions. *Phys. Rept.*, 481(1–2):1–28, September 2009. doi:10.1016/j.physrep.2009.07.004.

[42] K. Markovič and M. Viel. Lyman- forest and cosmic weak lensing in a warm dark matter universe. *Publ. Astron. Soc. Austral.*, 31, 2014. doi:10.1017/pasa.2013.43.

[43] R. Massey, T. Kitching, and J. Richard. The dark matter of gravitational lensing. *Rept. Prog. Phys.*, 73(8):086901, July 2010. doi:10.1088/0034-4885/73/8/086901.

[44] A. Merle. keV neutrino model building. *Int. J. Mod. Phys. D*, 22(10):1330020, 2013. doi:10.1142/S0218271813300206.

[45] D. Nelson et al. The IllustrisTNG simulations: public data release. *Comput. Astrophys. Cosmol.*, 6(1):2, 2019. doi:10.1186/s40668-019-0028-x.

[46] R. Nemiroff and J. Bonnell. Galaxy cluster Abell 370 and beyond. Astronomy Picture of the Day (APOD), NASA, May 2017. Accessed: October 2025. URL: https://apod.nasa.gov/apod/ap170506.html.

[47] C. A. J. O'Hare. Dark Matter Candidates. https://commons.wikimedia.org/wiki/File:Dark_matter_candidates.pdf, 2024. Licensed under CC BY 4.0. Accessed: Januray 2026.

[48] C. A. J. O'Hare. New definition of the neutrino floor for direct dark matter searches. *Phys. Rev. Lett.*, 127(25), December 2021. doi:10.1103/physrevlett.127.251802.

[49] R. Pakmor et al. The MillenniumTNG Project: the hydrodynamical full physics simulation and a first look at its galaxy clusters. *Mon. Not. Roy. Astron. Soc.*, 524(2):2539–2555, 07 2023. doi:10.1093/mnras/stac3620.

[50] A. A. Penzias and R. W. Wilson. A Measurement of Excess Antenna Temperature at 4080 Mc/s. , 142:419–421, July 1965. doi:10.1086/148307.

[51] N. P. Pitjev and E. V. Pitjeva. Constraints on dark matter in the solar system. *Astron. Lett.*, 39(3):141–149, March 2013. doi:10.1134/s1063773713020060.

[52] J. R. Primack and M. A. K. Gross. Hot dark matter in cosmology, 2001. doi:10.1007/978-3-662-04597-8_12.

[53] F. S. Queiroz. WIMP Theory Review. *PoS*, EPS-HEP2017:080, 2017. doi:10.22323/1.314.0080.

[54] V. C. Rubin and W. K. Ford, Jr. Rotation of the andromeda nebula from a spectroscopic survey of emission regions. *Astrophys. J.*, 159. doi:10.1086/150317.

[55] M. Schumann. Dual-phase liquid xenon detectors for dark matter searches. *JINST*, 9, 05 2014. doi:10.1088/1748-0221/9/08/C08004.

[56] M. Schumann. Direct detection of WIMP dark matter: concepts and status. *J. Phys. G*, 46(10):103003, aug 2019. doi:10.1088/1361-6471/ab2ea5.

[57] D. Scott and G. F. Smoot. Cosmic microwave background mini-review. 2024. arXiv:1005.0555.

[58] P. Sikivie. Experimental tests of the "invisible" Axion. *Phys. Rev. Lett.*, 51:1415–1417, Oct 1983. doi:10.1103/PhysRevLett.51.1415.

[59] G. F. Smoot et al. Structure in the COBE Differential Microwave Radiometer First-Year Maps. *Astrophys. J. Lett.*, 396:L1, September 1992. doi:10.1086/186504.

[60] V. Springel et al. Simulating the joint evolution of quasars, galaxies and their large-scale distribution. *Nature*, 435:629–636, 2005. doi:10.1038/nature03597.

[61] M. Thomas. Theory and phenomenology of CP violation. *Nucl. Phys. B Proc. Suppl.*, 167:115–119, 2007. doi:10.1016/j.nuclphysbps.2006.12.083.

[62] ULVAC CRYOGENICS INC. Cryocoolers — refrigerator. https://www.ulvac-cryo.com/products-en/refrigerator-en/cryocoolers/?lang=en. Accessed: February, 2026.

[63] W. Wang, J. Han, M. Cautun, Z. Li, and M. N. Ishigaki. The mass of our milky way. *Sci. China Phys. Mech. Astron.*, 63(10):109801. doi:10.1007/s11433-019-1541-6.

[64] R. H. Wechsler and J. L. Tinker. The connection between galaxies and their dark matter halos. *Ann. Rev. Astron. Astrophys*, 56(1):435–487, September 2018. doi:10.1146/annurev-astro-081817-051756.

[65] S. Weinberg. A new light boson? *Phys. Rev. Lett.*, 40:223–226, Jan 1978. doi:10.1103/PhysRevLett.40.223.

[66] XLZD Collaboration, J. Aalbers, et al. The XLZD Design Book: towards the next-generation liquid xenon observatory for dark matter and neutrino physics. *Eur. Phys. J. C*, 85(10):1192, 2025. doi:10.1140/epjc/s10052-025-14810-w.

[67] R. Yajur. Simulations for a 2.6 m tall dual-phase xenon time projection chamber. M.s. thesis, Indian Institute of Technology Madras, 2020.

[68] F. Zwicky. Die Rotverschiebung von extragalaktischen Nebeln. *Helv. Phys. Acta*, 6:110–127, 1933. doi:10.1007/s10714-008-0707-4.